

# 1 **Measurement Report: New particle formation characteristics** 2 **at an urban and a mountain station in Northern China**

3 Ying Zhou<sup>1</sup>, Simo Hakala<sup>2</sup>, Chao Yan<sup>1,2,\*</sup>, Yang Gao<sup>3</sup>, Xiaohong Yao<sup>3</sup>, Biwu Chu<sup>4</sup>, Tommy  
4 Chan<sup>2</sup>, Juha Kangasluoma<sup>1,2</sup>, Shahzad Gani<sup>2</sup>, Jenni Kontkanen<sup>2</sup>, Pauli Paasonen<sup>2</sup>, Yongchun  
5 Liu<sup>1</sup>, Tuukka Petäjä<sup>2,5</sup>, Markku Kulmala<sup>1,2</sup>, Lubna Dada<sup>2,6,7\*</sup>

6 <sup>1</sup> Aerosol and Haze Laboratory, Beijing Advanced Innovation Center for Soft Matter Science and  
7 Engineering, Beijing University of Chemical Technology, Beijing, China

8 <sup>2</sup> Institute for Atmospheric and Earth System Research / Physics, Faculty of Science, University of  
9 Helsinki, Finland

10 <sup>3</sup> Key Laboratory of Marine Environment and Ecology, Ministry of Education, Ocean University of  
11 China, Qingdao 266100, China

12 <sup>4</sup> State Key Joint Laboratory of Environment Simulation and Pollution Control, Research Center for  
13 Eco-Environmental Sciences, Chinese Academy of Sciences, Beijing 100085, China

14 <sup>5</sup> Joint International Research Laboratory of Atmospheric and Earth System Sciences (JirLATEST),  
15 Nanjing University, Nanjing, China

16 <sup>6</sup> Extreme Environments Research Laboratory, Ecole Polytechnique Fédérale de Lausanne (EPFL)  
17 Valais Wallis, Sion, 1951, Switzerland

18 <sup>7</sup> Laboratory of Atmospheric Chemistry, Paul Scherrer Institute, 5232 Villigen, Switzerland

19

20 \*Correspondence to: Lubna Dada: [lubna.dada@helsinki.fi](mailto:lubna.dada@helsinki.fi) & Chao Yan: [chao.yan@helsinki.fi](mailto:chao.yan@helsinki.fi)

## 21 **Abstract**

22 Atmospheric new particle formation (NPF) events have attracted increasing attention for their  
23 contribution to the global aerosol number budget, and therefore their effects on climate, air  
24 quality, and human health. NPF events are regarded as a regional phenomenon, occurring  
25 over a large area. Most observations on NPF events in Beijing and its vicinity were conducted  
26 in populated areas, whereas observations on NPF events ~~in~~ on mountain tops with ~~few~~ low

27 anthropogenic emissions are still rare in [BeijingChina](#) ([Wang et al. 2013](#)). The spatial  
28 variation of NPF event intensity has not been investigated in detail by incorporating both  
29 urban areas and mountain measurements in Beijing. Here, we provided NPF events  
30 characteristics in summers 2018 and 2019 at urban Beijing and a comparison of NPF event  
31 characteristics — NPF event frequency, ~~particle~~-formation rate, and growth rate — by  
32 comparing an urban Beijing site and a background mountain site separated by ~80 km from  
33 June 14 to July 14, 2019 as well as ~~give-giving~~ insights into the connection between both  
34 locations. There were no significant difference of ~~particle~~-formation rates and growth rates  
35 observed during the short-term observation in 2019 and longer-term observation in summers  
36 2018 and 2019 at the urban site. During parallel measurements at urban Beijing and mountain  
37 background areas, although the median condensation sink during the first two hours of the  
38 common NPF events was around  $0.01 \text{ s}^{-1}$  at both sites, there were notable differences in  
39 ~~particle~~-formation rates between the two locations (median of  $5.42 \text{ cm}^{-3}\text{s}^{-1}$  at the urban site  
40 and  $1.13 \text{ cm}^{-3}\text{s}^{-1}$  at the mountain site during the first two hours of common NPF events). In  
41 addition, the ~~particle~~-growth rates in the 7-15 nm range for common NPF events at urban site  
42 (median of  $7.6 \text{ nm.h}^{-1}$ ) ~~at the urban site~~ were slightly higher than those at mountain site  
43 (median of  $6.5 \text{ nm.h}^{-1}$ ). To understand whether the observed events were connected, we  
44 compared air mass trajectories as well as meteorological conditions at both stations.  
45 Favorable conditions for the occurrence of regional NPF events were largely affected by air  
46 mass transport. Overall, our results demonstrate a clear inhomogeneity of regional NPF  
47 within a distance of ~100 km possibly due to the discretely distributed emission sources.

48  
49 Keywords: atmospheric aerosols, growth rates, regional new particle formation, sulfuric acid

## 50 1 Introduction

51 Atmospheric new particle formation (NPF) events resulting from the formation of clusters  
52 and stable aerosol particles from gas-phase precursors have been recognized as a major  
53 contributor to the global aerosol budget (Kulmala et al., 2004; Zhang et al., 2012). Once the  
54 newly formed particles grow to certain sizes, they can act as cloud condensation nuclei

55 (CCN), affecting the regional and global climate (Pierce and Adams., 2009; Yu and Luo.,  
56 2009). NPF events were also found to contribute to haze formation and thus can influence air  
57 quality, especially in megacities where the precursor concentrations and associated *particle*  
58 formation rates are rather high (Guo et al., 2014; 2020; Kulmala et al., 2021; Du & Dada et al.,  
59 2021).

60 The occurrence of NPF events is a result of the competition between factors promoting and  
61 inhibiting cluster formation and their growth. For instance, sufficient sulfuric acid and other  
62 low-volatility vapors have been confirmed to be important in particle nucleation and growth  
63 in field observations as well as in chamber experiments (Ehn et al., 2014; Wang et al.,  
64 2017; Lehtipalo et al., 2018; Yao et al., 2018; Deng et al., 2020b). On the other hand,  
65 background particles can inhibit new particle formation by acting as condensation sink for  
66 vapor precursors and coagulation sink for newly formed particles. Indeed, Cai et al. (2017)  
67 found that the Fuchs Surface Area ( $A_{Fuchs}$ ) (which is linearly proportional to condensation  
68 sink) determined the occurrence of NPF events in urban Beijing. In the atmosphere, ambient  
69 conditions, such as air mass trajectories and meteorological conditions, can affect the  
70 occurrence of NPF events by modifying the source-sink competition. Wu et al. (2007)  
71 summarized favorable conditions for NPF events in Beijing based on a one-year observation  
72 as sufficient solar radiation (sunny days), northerly wind, low relative humidity, and less  
73 pre-loading large particles. Similarly, in other environments, plenty of radiation, intermediate  
74 temperatures and low condensation sink favor the occurrence of NPF events (Qi et al., 2015;  
75 Dada et al., 2017; Kerminen et al., 2018). Regional NPF events can happen with a spatial  
76 extent up to several hundred kilometers and vertical extent from boundary layer to free  
77 troposphere under favorable conditions (Hussein et al., 2009; Shen et al., 2011; Dai et al.,  
78 2017). Earlier studies have shown that regional NPF events by simultaneous observations at  
79 two or more sites had similar features in their occurrence and characteristics. For instance,  
80 Komppula et al. (2006) investigated the occurrence of NPF events at two forest stations in  
81 northern Finland during 2000-2003. Their results suggested that same air mass source regions,  
82 favorable weather conditions and clean air at both stations were necessary for NPF events

83 occurring simultaneously at the two stations. Vana et al. (2016) compared observations at  
84 three sites over 1000 km distance at northern Finland, southern Finland and Estonia in  
85 2013-2014. They found that some events have the same origin. On the other hand, Jun et al.  
86 (2014) observed that NPF events occurred less frequently at downtown Toronto than at a  
87 nearby background site, and attributed this observation to the high condensation and  
88 coagulation sink due to primary particle emission from traffic at urban areas. Moreover,  
89 Carnerero et al. (2018) observed horizontal distribution and regional impact of the NPF  
90 events with data from three urban, urban background, and suburban stations in the Madrid  
91 metropolitan area, Spain in July 2016. Their results indicated that ultra-fine particles were  
92 detected quasi-homogenously in an area spanning at least 17 km horizontally and the NPF  
93 events extended over the full vertical extension of the mixed layer. Finally, Salma et al. (2016)  
94 found that regional NPF events were modified and transformed by urban NPF events during  
95 their observation in 2008-2009 and 2012-2013 in Budapest and at a regional background site  
96 71 km away from it.

97 In comparison to the aforementioned studies in Europe, a similar study was also carried out to  
98 understand the regional NPF events in North China Plain. Wang et al. (2013) characterized  
99 the NPF events observed at an urban Beijing site and a regional background site about 120  
100 km northeast to the urban site from March to November in 2008. They observed 96 and 87  
101 NPF events at urban Beijing and background site, respectively, among which 52 NPF events  
102 were observed simultaneously at both sites. They found that NPF events were slightly weaker  
103 in the background site compared to those observed at the urban site. However, the factors that  
104 influence the occurrence of NPF events at the two stations simultaneously were left  
105 undetermined.

106 In addition to horizontal extension of NPF events, the vertical extension of NPF events also  
107 attract attention of researches. It have been confirmed that NPF events can be triggered  
108 within the whole low tropospheric column at the same time and even above the planetary  
109 boundary layer upper limit (Boulon et al., 2011). Sellegri et al. (2019) reviewed NPF events  
110 observed at 6 different altitude stations. They found NPF events was most favored at the

111 altitude close to the interface of the free troposphere (FT) with the planetary boundary layer  
112 (PBL) and at the vicinity with clouds. In addition, at high altitude sites, CS may not be the  
113 limiting factor for NPF occurrence as higher CS associated with more precursors for  
114 nucleation and initial growth. Based on observations at two different altitudes (e.g. 340 m and  
115 560 m above sea level) in northern Finland, Komppula et al. (2003) found NPF events had  
116 similar formation and growth rates between these two heights, while due to vertical  
117 movement of air masses, difference of NPF event start time between these two sites was  
118 limited within 30 min. Similar results were also observed at two sites in France that formation  
119 and growth rates were similar between two altitudes (e.g., 660 m and 1465 m above sea level)  
120 while the contribution of ion-induced nucleation was higher at high altitude (Boulon et al.,  
121 2011). Finally, during a recent observation in Spain, growth rates were higher at the mountain  
122 site (2500 m a.s.l.) than urban site (680 m a.s.l.), while difference between formation rates  
123 varied with altitude.

124 In addition to largely populated urban areas, there is a large mountain area within the  
125 Beijing-Tianjin-Hebei (BTH) region, where to our best knowledge, the characteristics of NPF  
126 events are understudied. In this study, we conducted simultaneous measurements of NPF  
127 event characteristics at an urban site in Beijing and a background mountain site about 80 km  
128 west to urban Beijing from June 14 to July 14 2019.

129 Based on our observations, we aim to (i) compare the characteristics of the NPF events  
130 between the two sites, including the frequency, ~~particle~~-formation rate, and ~~particle~~-growth  
131 rate; (ii) figure out the connections and differences between NPF events at these two sites; (iii)  
132 identify the ~~favoring~~-favorable conditions for regional NPF events. Due to the profound  
133 participation of NPF events in the global aerosol number loading and air quality degradation,  
134 identifying the conditions ~~that those~~ promote or inhibit the occurrence of regional scale NPF  
135 events could help to minimize its adverse effects.

136 **2 Experiment and methodology**

137 **2.1 *Measurement Sites' description***

138 Urban site: The Beijing University of Chemical Technology - BUCT (39.94° N, 116.31° E)  
139 station is located on the fifth floor of a university building inside the west campus of BUCT.  
140 The station is surrounded by several main roads with heavy traffic and residential areas and  
141 thus, can be considered a typical urban station. The altitude of the west campus of BUCT is  
142 around 20 m above sea level and the urban site is around 12 m above ground level. More  
143 details of this station can be found in Zhou et al. (2020). Observations at the urban site are  
144 continuous since January 17, 2018 and were only interrupted for necessary instrument  
145 maintenance. The location is referred to as 'UB' from here after and is shown on the map in  
146 Figure 1.

147 Mountain site: The Beijing Forest Ecosystem Research Station (39.96° N, 115.43° E) is  
148 located in the west of Beijing, referred to as 'MT' from here after, which is part of the  
149 Chinese Ecological Research Network (CERN). It is located in the mountain areas west of  
150 Beijing, about 80 km from the urban site; see also in Figure 1. The altitude of the station is  
151 1170 m above sea level and it is surrounded by forests. The closest anthropogenic activities  
152 are associated with small villages located in the valley nearby the MT station. Observations at  
153 MT station are from June 14 to July 14, 2019. For comparison reasons, we only used the data  
154 collected simultaneously at both stations.

155 Longquan station: The Longquan national monitoring station sits in Longquan town,  
156 Mengtougou District, Beijing. It is 20 km west to UB site and 60 km east to MT site and  
157 considered as a suburban station. The location is referred to as 'LQ' from here after and is  
158 shown on the map in Figure 1.

159 **2.2 *Instrumentation***

160 As shown in Figure 2, the data qualities of particle number size distribution at both sites  
161 during the short-term parallel observations was good in general. Particle number size

162 distribution data in the size range of 6-840 nm were collected using a differential mobility  
163 particle sizer (DMPS) at the UB station. The instrument consists of one Hauke-type DMA  
164 (differential mobility analyzer, home-built by university of Helsinki) in different flow rates  
165 and one CPC (condensation particle counter, TSI Model 3772). Details of this instrument can  
166 be found in Salma et al. (2011) and Kangasluoma et al. (2020). At MT station, a scanning  
167 mobility particle sizer (SMPS, consists of a TSI Differential Mobility Analyzer model 3081)  
168 and a fast mobility particle sizer (FMPS, TSI Model 3091) were used to measure particle  
169 number size distribution from June 14 to June 28 and from June 29 to July 14, respectively.  
170 The size ranges of the SMPS and FMPS are 7-1218 nm and 6.04-856 nm, respectively. The  
171 total number concentration from 4-3000 nm, measured by Condensation Particle Counter  
172 (CPC; TSI Model 3775), was used to calibrate the particle number size distributions from  
173 FMPS according to the method suggested by Zimmerman et al. (2015). More details about  
174 the instrument are found in the previous studies (Wang et al., 2019; Gao et al., 2020). ~~The full~~  
175 ~~campaign particle number size distributions at both sites are shown in Fig. 2.~~ The particle  
176 number size distribution measured by FMPS correlated well with SMPS during the  
177 comparison in laboratory after being calibrated (Lee et al., 2013).

178 To ensure high quality of particle number size distribution data at UB site, a particle number  
179 size distribution system (PSD) also sampled in parallel with DMPS from June 1 to August 31,  
180 2019 (summer 2019). It included a nano-scanning mobility particle sizer (nano-SMPS, 3–55  
181 nm, mobility diameter), a long SMPS (25–650 nm, mobility diameter) and an aerodynamic  
182 particle sizer (APS, 0.55–10  $\mu\text{m}$ , aerodynamic diameter). Details of this instrument can be  
183 seen at Liu et al. (2016) and Deng et al. (2020b).

184 The PSD was used as a reference. As shown in Figure 3, median particle number size  
185 distribution obtained from PSD and DMPS matched well ~~with each other within a factor of 2~~  
186 ~~during our observation in summer 2018 and 2019 at UB site~~ in data trend. Varying with  
187 particle diameter, particle number size distribution data measured by DMPS can be higher or  
188 lower than PSD within a factor of 2.

189 We cannot compare particle number size distribution data obtained from DMPS, SMPS and

190 FMPS as we did not sample with these three instruments in parallel at the same site.  
191 However, it is reasonable to assume that particle number size distribution obtained from  
192 FMPS were comparable with those from DMPS as on one hand the measurement techniques  
193 of particle number size distribution in the size range of these two instruments have been well  
194 developed and be applied in quite a lot observations (Wang et al., 2017; Kangasluoma et al.,  
195 2020), on the other hand, the particle number size distribution from FMPS was carefully  
196 calibrated and the FMPS was properly operated during the observation as discussed above.  
197 Similar conclusions apply for the SMPS as well where we can rely on using the measurement  
198 from this instrument to discuss at least NPF event frequency at MT site during June 14 to  
199 June 28, 2019, during which parameters of only one NPF event are calculated.

200 Sulfur dioxide (SO<sub>2</sub>) concentration data were collected by Thermo Environmental Instrument  
201 model 43i-TLE with a time resolution of 5-min at the UB station. There were no direct  
202 measurement of SO<sub>2</sub> concentrations at the MT station, but the SO<sub>2</sub> measurement at the closest  
203 national monitoring station (Longquan station, around 60 km from MT station and 20 km  
204 from UB station, see Figure- 1) was used to indicate the strong decline of SO<sub>2</sub> concentration  
205 from urban Beijing towards the west areas. Time series of SO<sub>2</sub> concentration at UB station  
206 and Longquan station during the whole observation is shown in Fig-ure 4. Due to the lower  
207 emission, the SO<sub>2</sub> concentration at the MT station is expected to be even lower than that in  
208 Longquan station.

209 The sulfuric acid concentration was measured at UB station by a chemical  
210 ionization-atmospheric interface-time of flight mass spectrometers (CI-APi-ToF, Aerodyne  
211 Research Inc.) equipped with a nitrate chemical ionization at UB station (Lu et al., 2019).  
212 There were no sulfuric acid data available at MT station and since no SO<sub>2</sub> concentrations  
213 were available, a sulfuric acid proxy concentration could not be derived.

214 The meteorological conditions such as relative humidity (RH, %), temperature (°C) and solar  
215 radiation (UVA and UVB, W/m<sup>2</sup>) were measured using a Vaisala Weather station data  
216 acquisition system (AWS310, PWD22, CL51), Metcon at UB station and using Vaisala  
217 MAWS301 automatic weather station at MT station. The measurements at the MT station



218 were carried out at the height of 1.5 m. The wind speed (m/s) and wind direction (°) data ~~is~~  
219 were also measured by the weather station at UB site, while at MT site, we obtained with  
220 reanalyzed data from ERA5 model (Olauson, 2018).

### 221 **2.3 Air mass back trajectories**

222 Air mass back trajectories were calculated using a Lagrangian particle dispersion model  
223 FLEXPART (FLEXible PARTicle dispersion model) version 9.02 (Stohl et al., 2005). As the  
224 meteorological input, we used ECMWF (European Centre for Medium-Range Weather  
225 Forecast) operational forecast data with 0.15° horizontal and 1-hour temporal resolution.  
226 Particle retrorplume simulations were performed hourly for both sites during the whole study  
227 period. For each retrorplume simulation, we used 50 000 model particles distributed evenly  
228 between 0–100 m above the measurement site. The released model particles were traced  
229 backwards in time for 72 h, unless they exceeded the model grid (20–60°N, 95–135°E,  
230 resolution: 0.05°).

231 Based on the arrival direction of the 72-h backward trajectories, the prevailing air mass  
232 transport conditions at each site were classified into 5 groups: North group, West group, East  
233 group, South group and Local group. Air masses arriving from north, north-west and  
234 north-east including Mongolia, Inner-Mongolia and north-east China were classified into the  
235 North group. Air masses from Shanxi province, Inner-Mongolia and further west were  
236 classified into the West group. Air masses from the ocean east of Beijing were classified into  
237 the East group and air masses from southern areas were classified into the South group.  
238 Stagnant air masses that had only travelled short distances and/or were circulating around the  
239 measurement site were classified into the Local group. Examples of air mass trajectories  
240 belonging to these five groups are shown in Figure 5. In general, air masses from the north  
241 and west supply clean air from the mountainous areas to both stations, whereas air masses  
242 from the east and south travel over highly populated areas, thus accumulating air pollutants.  
243 However, the impact of local air masses on the pollution levels at the two sites can be  
244 different; at UB station, local air masses are polluted by the urban emissions, while at MT

245 station stagnant air could cause a clean situation due to low local emissions. More details on  
246 the relationship between air mass transport conditions and the extent of pollution is discussed  
247 in later sections.

#### 248 **2.4 Estimating the spatial extent of NPF**

249 The observation of regional new particle formation events, where the growth of newly  
250 formed particles can be followed for several hours, is a result of NPF taking place over a  
251 large spatial area. This is because as time progresses, the particles observed at a measurement  
252 site ~~should~~ ~~must~~ have originated from further and further away due to non-zero wind  
253 conditions. Following the progression of the observed NPF event and using air mass back  
254 trajectories, we can estimate where the particles observed at different stages of the NPF event  
255 were initially formed by calculating the air mass locations at the onset time of the NPF event  
256 (assuming that NPF occurs simultaneously over the larger area). Typically, the mode related  
257 to the NPF event disappears from the observations after some time. This is an indication of  
258 the currently observed air mass arriving from an area where NPF was no longer taking place  
259 due to unfavorable local conditions. If the shift in the air mass origin towards unfavorable  
260 conditions occurs gradually over time, the mode related to the NPF event can enter a stage of  
261 growth stagnation (or even decrease in size) before disappearing completely (Kivekäs et al.,  
262 2016). This is because the increasing transport time between NPF onset and observation of  
263 the particles at the measurement site provides less and less additional ‘material’ for aerosol  
264 growth towards the more unfavorable conditions. Calculating the locations where NPF is  
265 assumed to have taken place for longer data sets including several regional NPF events can  
266 give an estimation of the typical spatial extent of NPF around the measurement location. It  
267 should be noted that even in relatively clear cases, the subjective determination of NPF event  
268 onset and end times can easily lead to uncertainties of few tens of kilometers in the  
269 estimations. In locations with strong primary pollution sources, such as urban Beijing,  
270 objective determination of NPF event start and stop times ~~said times~~ becomes even more  
271 difficult. More details and discussion related to the method and its uncertainties can be found  
272 in Kristensson et al. (2014).

## 273 2.5 NPF event classification

274 Particle number size distribution data from both stations were used for classifying individual  
275 days into new particle formation (NPF) event days and non-event days. This classification  
276 followed procedures presented by Dal Maso et al. (2005) and later adapted for urban  
277 locations (Chu et al., 2021) in which a day is classified as a NPF event day if (a) a new mode  
278 in the size range smaller than 25 nm appeared and (b) the new mode kept growing over  
279 several hours. On the other hand, non-event days are the days which do not fit any of the  
280 abovementioned criteria and undefined days are the days which fit either one of the  
281 abovementioned criteria ~~or the days which we cannot distinguish whether the new mode was~~  
282 ~~from NPF event or traffic.~~ At UB site, we also observed some cases in which nucleation  
283 mode particle number concentration burst without mode diameter increase. It could be related  
284 to non-regional NPF events (Dai et al., 2017). We did not observe such cases at the MT site.  
285 Actually, the abundant anthropogenic emissions in the megacity could provide enough  
286 precursors for non-regional NPF events. However, traffic emissions can also provide  
287 abundant primary nucleation mode particles, making it difficult to distinguish whether the  
288 new mode was from NPF event or traffic. So we classified such events as “undefined” also.

## 289 2.6 Characteristics of NPF events

### 290 2.6.1 Condensation sink

291 The condensation sink (CS) was calculated from particle size distribution data using the  
292 method described by Kulmala et al. (2012):

$$293 \quad CS = 2\pi D \sum_{dp'} \beta_{m,dp'} dp' N_{dp'}$$

294 (1)

295 where  $D$  is the diffusion coefficient of the condensing vapor, sulfuric acid in our case, and  
296  $\beta_{m,dp'}$  represents the transition-regime correction,  $N_{dp'}$  is the particle number concentration  
297 with diameter  $dp'$ . As shown in Fig-~~ure~~ 6, particles in size range of 20-800 nm dominated the  
298 total CS at UB station and particles in the size range of 50-800 nm dominated the total CS at

299 MT station. Although the size ranges of DMPS, FMPS and SMPS slightly differ, all of them  
300 cover the main size range which constituted the CS and thus the calculation of CS should not  
301 be significantly influenced by differences in the instrument size ranges.

302 As shown in Figure 6(c&e) on NPF event days, particles smaller than 100 nm built a CS of  
303  $3.7 \times 10^{-3} \text{ s}^{-1}$ , contributing 37% to the total CS. While at MT site, particles smaller than 100  
304 nm only built a CS of  $1.2 \times 10^{-3} \text{ s}^{-1}$ , contributing less than 12% to the total CS (Figure 6 (d&f)).  
305 Although 100-840 nm particle number concentration at UB site was much less than that at  
306 MT site, 1-100 nm (especially 25-100 nm) particles compensated total CS by higher number  
307 concentration on NPF event days (CS at each site will be discussed in section 3.1.2 ).

308 The data on rainy days were discarded from analysis at both sites, hence the precipitation was  
309 considered to have minor effects on our CS calculation. We calculated CS at both sites  
310 assuming RH as 0%. It should be noted that the CS may have been underestimated by a factor  
311 of 1.12-1.33 at MT site when we include RH in the CS calculation, e.g. 30%-70% during  
312 9:00-15:00, as shown in Figure 10 and Figure S1.

### 313 2.6.2 Particle growth rates

314 Particle growth Growth rates were calculated for the size range of 7-15 nm ( $GR_{7-15 \text{ nm}}$ ) using  
315 the 50% appearance time method introduced by Lehtipalo et al. (2014) and Dada et al. (2020a)  
316 according to

$$317 \quad GR = \frac{dp_2 - dp_1}{t_2 - t_1}$$

318 (2)

319 where  $t_2$  and  $t_1$  are the appearance times of particles with sizes of  $dp_2$  and  $dp_1$ , respectively.  
320 The appearance time is defined as the time at which the concentration of particles at size  $d_p$   
321 reaches 50% of its maximum.

### 322 2.6.3 Particle formation rates

323 The formation rates of particles of diameters 7 nm ( $J_7$ ) were calculated from particle number

324 size distribution data using the method presented by Kulmala et al. (2012) and modified for  
 325 urban environments by Cai and Jiang (2017):

$$\begin{aligned}
 J_k = & \frac{dN_{[d_k, d_u]}}{dt} + \sum_{d_g=d_i}^{d_u} \sum_{d_i=d_{min}}^{+\infty} \beta_{(i,g)} N_{[d_i, d_{i+1})} - \frac{1}{2} \sum_{d_g=d_{min}}^{d_u} \sum_{d_i^2=\max(d_{min}^2, d_k^2-d_{min}^2)}^{d_{i+1}^2+d_{g+1}^2 \leq d_u^2} \beta_{(i,g)} N_{[d_i, d_{i+1})} N_{[d_g, d_{g+1})} \\
 & + \left. \frac{dN}{dd_i} \right|_{d_i=d_u} \bullet GR_u
 \end{aligned}
 \tag{3}$$

328 Here,  $J_k$  is the ~~particle~~ formation rate at size  $d_k$ ,  $\text{cm}^3 \cdot \text{s}^{-1}$ , (7 nm in this study);  $d_u$  is the upper  
 329 size limit of the targeted aerosol population (10 nm in this study);  $d_{min}$  is the smallest particle  
 330 size detected by particle size spectrometers (to make the results comparable, the  $d_{min}$  was set  
 331 to 7 nm);  $N_{[d_k, d_u]}$  is the number concentration of particles from size  $d_k$  to  $d_u$  (particles with  
 332 diameters of  $d_u$  are not accounted for);  $d_i$  represents the lower limit of the  $i^{\text{th}}$  size bin;  $\beta_{(i,g)}$  is  
 333 the coagulation coefficient for the collision of two particles with the size of  $d_i$  and  $d_g$ ; and  $GR_u$   
 334 refers to the ~~particle~~ growth rate at size  $d_u$ ,  $\text{nm} \cdot \text{h}^{-1}$  Deng et al. (2020b).

335 3—Determination of nucleation start and stop times was affected by traffic emissions at UB  
 336 station. Hence, we chose a time window of the first 2 hours of NPF event for formation rates  
 337 calculation at both sites. During the time window, we always observed 7-10 nm particle  
 338 number concentration burst significantly from the background level at both sites.

339

Formatted: Normal

340 **3 Results and discussion**

341 ~~NPF event frequencies at both stations~~3.1 Origin of NPF events at both sites

342

343 During our observation in summer 2018 and 2019 (from June to August of each year) at UB  
344 station, there were 155 days with valid data, 53 days of which were classified as NPF event  
345 days, corresponding to an NPF event frequency of 34%. This NPF event frequency was  
346 consistent with an earlier observations in summer in urban Beijing ~~in from 2004 and to 2008~~  
347 ~~in summer~~ while smaller than other seasons especially winter during ~~and the that~~ observation  
348 and another one-year observation in UB station (Wu et al., 2007; Wang et al., 2013;Deng et  
349 al., 2020b).

350 For comparison of NPF ~~characters~~characteristics between UB and MT stations, a parallel  
351 short-term observation was conducted at MT station from June 15 to July 14, 2019. In Fig-ure  
352 2, we show the particle number size distribution and CS during our short-term observations at  
353 both stations. There were a total of 12 and 13 NPF events observed at the UB station and the  
354 MT station, corresponding to an NPF event frequency of 48% (12 of 25) and 52% (13 of 25),  
355 respectively. Data were considered as valid when visual inspection of the particle number size  
356 distribution data and the instrument status did not indicate problems in the measurements.  
357 Only days with valid data at both stations were taken into consideration in our analysis. Only  
358 days when particle number size distribution data were valid that visual inspection of the data  
359 and the number concentrations as well as instrument status do not indicate problems in the  
360 measurements for both stations were taken into consideration in our analysis. In addition, 9  
361 NPF events were observed at both stations on the same day (referred to as common NPF  
362 events). Detailed information on the classified NPF event and non-event days, including the  
363 ~~particle~~ formation rates, growth rates, as well as their associated air mass origins during the  
364 short-term observation are provided in Table 1.

365 In order to understand the conditions favoring NPF events at both stations, we analyzed

Formatted: Heading 2, Space Before: 0 pt, After: 0 pt

Formatted: Indent: Before: 0 cm, Hanging: 1.02 cm

366 various ambient parameters including air mass trajectories, meteorological variables,  
367 condensation sink as well as sulfuric acid concentration.

### 368 3.1.1 Favorable air mass origin for NPF events at individual locations

369 In [Figure 7](#), we show frequencies of air masses arriving at UB station from different  
370 directions during our observation in summer 2018 and 2019. The most frequent air masses  
371 arriving at UB station belonged to the South group. During our observation in the two  
372 summers, out of 155 days were 52 days belonging to the South group and 39, 32, 9 and 23  
373 days in air masses belong to North, East, West and Local groups, respectively. NPF event  
374 frequency with respect to air masses is also shown in [Figure 7](#). It is noticeable that air mass  
375 origin influenced the occurrence of NPF events at UB site as the majority of NPF events  
376 occurred when the air masses were coming from the north. During our observation in summer  
377 2018 and 2019, 34 (out of 55) NPF events occurred in air masses from the North group and 9,  
378 2, 2 and 6 NPF events in the South, East, West and Local groups, respectively ([Figure 7a](#)).  
379 One prominent feature of these air masses is their difference in CS. The CS of the air masses  
380 classified as the North group (with median values of  $0.01 \text{ s}^{-1}$  at UB station) is substantially  
381 lower than that in other air mass classes (CS = 0.03, 0.025, 0.017,  $0.03 \text{ s}^{-1}$ , for south, east,  
382 west and local, respectively), which might explain the high NPF event frequency associated  
383 with this air mass class. During the observation from June 14 to July 14 in summer 2019, the  
384 most frequent air masses arriving at both sites belonged to the North group as shown in [Table](#)  
385 1. Out of 25 days, there were 8 and 9 days belonging to the North group, at UB and MT sites,  
386 respectively. The highest frequency of NPF events also occurred when the air masses were  
387 coming from the north. The high NPF events frequency during our observation from June 14  
388 to July 14 could also be attributed to the frequent air masses arriving at both sites from north  
389 to Beijing.

390 As shown in [Table 1](#), NPF events occurring simultaneously at both sites only happened when  
391 air masses arrived at both sites from the same directions, suggesting that most of the observed  
392 NPF events took place over the whole studied area, extending for several hundreds of  
393 kilometers (Dai et al., 2017; Du et al., 2021). The occurrences of common NPF events also

394 closely connected with air mass origins that 7 (out of 9) common NPF events occurred under  
395 air masses in the North group, with the other two NPF events in the South group.

### 396 3.1.2 The role of condensation sink in NPF event occurrence

397 Figure 8a shows the difference in CS between NPF event and non-event days during our  
398 observation in summer 2018 and 2019 (two whole summers) at UB site and short-term  
399 parallel observations at both sites. The ‘NPF1’ and ‘non-event1’ referred to NPF and  
400 non-event days during the two whole summers, respectively, while ‘NPF2’ and ‘non-event2’  
401 referred to NPF and non-event days during the short-term parallel observation period from  
402 June 14 to July 14, 2019 at both sites, respectively. The longer-term periods are used for  
403 confirming the representativeness of the short-term overlapping period for the whole summer.

404 As shown in ~~the figure~~Figure 8a, the median CS on NPF1 or NPF2 days is equivalent for UB  
405 station ( $CS_{\text{NPF1}} = 0.010\text{s}^{-1}$ ;  $CS_{\text{NPF2}} = 0.009\text{s}^{-1}$ ) and less than a factor of 1.2 different between  
406 non-event1 and non-event2 in UB station ( $CS_{\text{nonevent1}} = 0.023\text{s}^{-1}$ ;  $CS_{\text{nonevent2}} = 0.020\text{s}^{-1}$ ), which  
407 confirms the representativeness of our short-term measurement period to the overall urban  
408 Beijing summer.

409 Our results in ~~figure~~Figure 8a show that the median CS was  $\sim 0.01\text{ s}^{-1}$  during the first 2 hours  
410 of the NPF events, at both stations. On common NPF event days, the median CS was  $0.009$   
411  $\text{s}^{-1}$  at UB station and  $\sim 0.01\text{s}^{-1}$  at MT station, respectively. In comparison, on non-event days,  
412 during roughly the same time period (9:00–11:00 LT), the CS was substantially higher, with  
413 median values of  $0.02\text{ s}^{-1}$  and  $0.014\text{ s}^{-1}$ , at UB and MT stations, respectively. Figure 8b  
414 presents the median CS during the first 2 hours of NPF events on common NPF event days  
415 measured at both stations, and shows the high correlation between the two.

416 Figure 8c shows the NPF event frequency as a function of CS during our observation at UB  
417 site in summer 2018 and 2019 and how the NPF event frequency decreased with increasing  
418 CS. When CS was smaller than  $0.01\text{ s}^{-1}$ , all days were classified as NPF event days, and when  
419 CS was larger than  $0.035\text{ s}^{-1}$ , no day was classified as NPF event day. This shows the major  
420 role of background particles in controlling the occurrence or inhibition of NPF events as  
421 shown in several previous studies in China and internationally (Deng et al., 2020a; Cai et al.,



422 2017; Kulmala et al., 2017). While we cannot present a similar figure from the MT station,  
423 the same conclusion applies where CS does play a role in inhibiting NPF observation owing  
424 to the difference in the CS values observed between NPF and nonevents at MT as shown in  
425 figure 8a. Yet, since the overall preexisting particle concentration at the MT is rather on the  
426 low end, the role of CS might not be as vital at the MT station as for the UB station.

427 Different from NPF events under low CS ( $<0.01 \text{ s}^{-1}$ ), these NPF events under high CS were  
428 characterized by a relatively high  $\text{H}_2\text{SO}_4$  concentration ( $>10^7 \text{ cm}^{-3}$ ) or low ~~particle~~-formation  
429 rates (Figure 9a), discussed in further details in the coming sections. In comparison, at MT  
430 station, when CS was smaller than  $\sim 0.013 \text{ s}^{-1}$ , most (10 out of 14) days were classified as  
431 NPF event days as shown in Figure 9d. When CS was larger than  $\sim 0.013 \text{ s}^{-1}$ , we only  
432 observed one local NPF event and another two non-local NPF events (Table 1). The local  
433 NPF event under high CS at the MT station was characterized as high UV ( $>30 \text{ W/m}^2$ ) and  
434 low formation rate ( $J_7$  were too small to be reliably calculated) as well.

### 435 3.1.3 Role of meteorological variables in NPF event occurrence

436 While the air mass source regions, and their connection to the CS, seem to explain the general  
437 picture of NPF event occurrences at the two sites well, we still have some cases unexplained.  
438 For example, as shown in Table 1, there were several non-event days observed at MT station  
439 with air masses belonging to North and West groups, which were connected to low CS. This  
440 indicates that a further investigation into other NPF-related variables is still required.

441 In Figure 10, we show diurnal variation of meteorological variables during our observation in  
442 summer 2018 and 2019 at UB site and observations from June 14 to July 14 in 2019 at UB  
443 and MT sites. It is noticeable that the short-term observation compared well with the  
444 long-term observation and therefore is representative of summer at UB site as shown in  
445 Figure 10.

446 First, the intensity of solar radiation is considered to be one of the most important parameters  
447 deciding NPF event occurrence as it translates into photochemistry strength (Chu et al., 2019).  
448 The median UV (UVA+UVB) intensity at the UB station on NPF event and non-event days  
449 was 38.3 and 32.9  $\text{W/m}^2$ , respectively. The UV intensity was on average  $\sim 15\%$  higher on

450 NPF event days than on non-event days at UB station. Although UV intensity was important  
451 for NPF event occurrence, we still observed NPF events at UB station under low UV intensity,  
452 e.g. cases on June 30 and July 6. These two events all started immediately after sunrise (6:30  
453 LT on June 30 and 7:00 LT on July 6, see Table 1) and median UV intensity during the first  
454 two hours of NPF events was only 13.2 and 14.1 W/m<sup>2</sup>, respectively. However, sulfuric acid  
455 concentration was higher than 10<sup>7</sup> cm<sup>-3</sup> at the same time, the possible reason is high SO<sub>2</sub>  
456 concentration and low CS (~0.003 s<sup>-1</sup>) outcompeted the low UV intensity (Dada et al., 2020b)  
457 as well as the possibility of having other H<sub>2</sub>SO<sub>4</sub> sources (Yao et al., 2020).

458 At MT station, the median UV intensity on NPF event and non-event days was 28.4 and 14.2  
459 W/m<sup>2</sup>, respectively. The lower UV at MT station, in general might be related to the higher  
460 RH (Fig-[ure 10c&d](#)) and thus more cloudiness and fog at the MT station (Hamed et al.,  
461 2010;Dada et al., 2018). The UV intensity was on average ~100% higher on NPF event days  
462 than on non-event days at UB station. All local NPF events happened when UV intensity was  
463 higher than 15 W/m<sup>2</sup> as shown in Fig-[ure 9d](#).

464 On the other hand, as shown in Fig-[ure 10c&d](#), the median relative humidity (RH) was lower  
465 on NPF event days than non-event days at both stations. This is consistent with earlier results  
466 that high RH suppressed NPF events by increasing CS and coagulation sink (CoagS), as it  
467 can enhance the particle hygroscopic growth (Hamed et al., 2010; Hamed et al., 2011). In  
468 addition, high RH was also found to be associated with more clouds resulting in less solar  
469 radiation (Dada et al., 2018).

470 The median temperatures at UB on event and non-event days were 31 °C and 29 °C,  
471 respectively, and at MT station 23 °C and 19 °C, respectively. The median temperature was  
472 lower at the MT station than at the UB station, due to the higher altitude of the station and  
473 likely also the weaker solar radiation (Fig-[ure 10e&f](#)). At both stations, the median  
474 temperature was very similar on NPF event and non-event days, suggesting that temperature  
475 was not a crucial factor for NPF event occurrence during the measurement in summer.

#### 476 *3.1.4 Role of sulfuric acid concentrations in NPF event occurrence*

477 Sulfuric acid has been found to be the main precursor vapor participating in NPF in China

478 and in many locations around the world due to its low volatility (Yao et al., 2018; Chu et al.,  
479 2019). In Fig-[ure 9a](#), we show the concentration of sulfuric acid as a function of CS during  
480 summer 2018 and 2019 at UB site. As shown in Fig-[ure 9b](#), the median sulfuric acid ( $\text{H}_2\text{SO}_4$ )  
481 concentrations at UB station were  $8.1 \times 10^6 \text{ cm}^{-3}$  and  $4.5 \times 10^6 \text{ cm}^{-3}$  on NPF event days and  
482 non-event days, respectively, during observation from June 14 to July 14 in 2019 and  $7.9 \times 10^6$   
483  $\text{cm}^{-3}$  and  $3.4 \times 10^6 \text{ cm}^{-3}$  on NPF event days and non-event days, respectively, during the  
484 observation in summer 2018 and 2019. This suggests that  $\text{H}_2\text{SO}_4$  was important for NPF  
485 events at the UB station (Deng et al., 2020b; Dada et al., 2020b). On the other hand, as shown  
486 in Fig-[ure 9a](#), the  $\text{H}_2\text{SO}_4$  concentration during 9:00- 11:00 (local time) on non-event days  
487 could be comparable with that on NPF event days, especially when CS was high. The  $\text{H}_2\text{SO}_4$   
488 concentration during 9:00- 11:00 (local time) on non-event days could be comparable with  
489 that on NPF event days, especially when CS was high. Altogether, our observation shows that  
490 the occurrence of NPF events was controlled by both  $\text{H}_2\text{SO}_4$  and CS at the UB station (Cai et  
491 al., 2020).

492 In addition, although we did not perform the measurement of  $\text{H}_2\text{SO}_4$  at the MT station,  
493 concentration of  $\text{H}_2\text{SO}_4$  is expected to be much lower than that at the UB station. First, the  
494  $\text{SO}_2$  concentration at measurement at Longquan Town was always below the detection limit  
495 ( $\sim 0.5$  ppb) during our observation period. In comparison, median  $\text{SO}_2$  concentration at UB  
496 station was 0.87 ppb for all days and 0.65 ppb for NPF event days during our short-term  
497 parallel observation period. The spatial decreasing trend of  $\text{SO}_2$  concentration from urban  
498 Beijing to the west implies a low  $\text{SO}_2$  concentration at the MT station, especially when the  
499 nearby anthropogenic sources are sparse (Liu, 2008; Ying, 2010; Wang, 2011; Yang-Chun et  
500 al., 2013). Second, the oxidation of  $\text{SO}_2$  by photochemistry reactions could also be limited by  
501 the low solar radiation at the MT station as we discussed in 3.1.3. Third, CS, as the main sink  
502 of  $\text{H}_2\text{SO}_4$ , was comparable at the MT station to that in the UB station on NPF event days (as  
503 shown in Fig-[ure 8a](#)). Altogether, the lower production rate and the equivalent loss rate of  
504  $\text{H}_2\text{SO}_4$  at the MT station likely results in the lower  $\text{H}_2\text{SO}_4$  concentration, in comparison to  
505 UB station.

506 Due to the lack of H<sub>2</sub>SO<sub>4</sub> measurements, the NPF mechanism at the MT station cannot be  
507 inferred. Nevertheless, we show that the occurrence of NPF ~~as~~is a response to  
508 photochemistry (and very likely to H<sub>2</sub>SO<sub>4</sub>) and CS in Fig-~~ure~~ure 9d. It is clear that high UV  
509 intensity and low CS favored the occurrence of NPF. However, there existed exceptions. For  
510 example, two NPF events were observed even when the UV intensity was low and the CS  
511 was high, besides, it was an undefined day on June 28 despite of the high UV intensity and  
512 low CS. These exceptional cases will be discussed in detail in Section 3.6.1 and 3.6.2,  
513 respectively.

### 514 **3.2 NPF event start time at both stations**

515 There was no significant difference in NPF event start times between the long-term and  
516 short-term parallel observations at UB site. In this section, we only compare NPF event start  
517 times of ~~common events~~coincident events at UB and MT sites during the short-term parallel  
518 observations.

519 During our observation, there was no advection of air masses between the two sites on  
520 common NPF event days, indicating that the NPF events occurred at each site independently.

521 As shown in Table 1, all common NPF events started after sunrise and prior to noon except  
522 the two non-local NPF events at MT station. However, NPF event start time was different  
523 between the two sites. Earlier researches in Nanjing, China and Nordic stations showed the  
524 similar results that NPF events can be observed simultaneously at two or more sites, but the  
525 start time can be different, local meteorology, source strength and background aerosols could  
526 drive temporal behavior of NPF events at each sites (Hussein et al., 2009; Dai et al., 2017).

### 527 **3.3 Particle formation and growth rates at both stations**

528 The ~~particle~~-formation rates ( $J_7$ ) at the two stations during the measurements are presented in  
529 Fig-~~ure~~ure 11a.  $J_7$  observed during the short-term parallel observation (NPF2) at UB site ~~was~~  
530 were in the range of 3.0-10.0 cm<sup>-3</sup> s<sup>-1</sup> with a median of 5.4 cm<sup>-3</sup> s<sup>-1</sup>, comparable with those  
531 observed in summer 2018 and 2019 (NPF1 = 2-14.0 cm<sup>-3</sup> s<sup>-1</sup> with a median of 4.9 cm<sup>-3</sup> s<sup>-1</sup>)

532 and significantly higher than the values in the MT station ( $0.75\text{-}3.0\text{ cm}^{-3}\text{s}^{-1}$  with a median of  
533  $0.82\text{ cm}^{-3}\text{s}^{-1}$ ) for common NPF events (Figure 11b). These values are comparable to earlier  
534 observations in urban Beijing and another regional background station in North China Plain  
535 (NCP) (Wang et al., 2013). Earlier observations in NCP and Yangtze River Plain also  
536 ~~observed show~~ higher formation rates at urban sites than corresponding background sites by  
537 roughly a factor of 2 due to lower anthropogenic emissions at background sites (Wang et al.,  
538 2013; Dai et al., 2017; Shen et al., 2018). The much lower  $J_7$  observed at MT station is very  
539 likely associated with the low  $\text{H}_2\text{SO}_4$  concentration at this station, as we discussed above.  
540 However, other reasons, such as the low concentration of  $\text{H}_2\text{SO}_4$  stabilizers, e.g., amines,  
541 cannot be ruled out either. Also, the  $J_7$  at UB station could be affected by particle emissions  
542 due to the proximity of the location to the highway, while compared with NPF events, the  
543 effect of traffic emissions is shown to be minor (Kontkanen et al., 2020; Zhou et al., 2020). In  
544 addition, Boulon et al. (2011) observed that new particles could be formed at low altitude and  
545 transported to the higher altitude sites, however, to confirm whether the phenomenon can  
546 happen at MT site, we still need observation on vertical wind conditions or vertical evolution  
547 of potential temperature.  
548 The ~~particle~~-growth rates in size range of 7-15 nm ( $\text{GR}_{7-15\text{nm}}$ ) at the UB station (4.8-12.9  
549 nm/h with a median of 7.8 nm/h) during NPF2 was also comparable with the whole summers  
550 (NPF1) (4.8-12.9 nm/h with a median of 8.5 nm/h). While the difference in  $J_7$  was 7 times  
551 higher in UB than in MT, the observed GR were only a slightly higher at UB than at the MT  
552 station (5.7-10.5 nm/h with a median of 6.5 nm/h) for common NPF events (Figure 11c&d),  
553 implying that precursors needed for particle formation were much more abundant in the  
554 polluted urban environment (Wang et al., 2013), while those needed for growth are rather  
555 comparable. The GR at UB station was comparable ~~with to~~ other long-term observation at  
556 UB station (1.1-8.0 nm/h) in 2018, and other urban areas in China (Herrmann et al.,  
557 2014; Chu et al., 2019; Deng et al., 2020b). Consistent with earlier observations showing that  
558  $\text{H}_2\text{SO}_4$  could only contribute to a small fraction of the particle growth ~~at in~~ this size range  
559 (Paasonen et al., 2018; Qi et al., 2018; Guo et al., 2020), the growth rates at both stations

560 cannot be explained by the H<sub>2</sub>SO<sub>4</sub> concentration. This implies that other condensable species,  
561 very likely low-volatility organic vapors, play an important role in particle growth at both  
562 stations. At the UB station, anthropogenic VOCs are dominant precursors of these  
563 low-volatility organic vapors (Guo et al., 2020; Deng et al., 2020a), while VOCs at MT  
564 station, with rare anthropogenic sources, are likely dominated by biogenic emissions.

### 565 *3.4 Ending diameters of newly-formed grown particles*

566 Earlier observations have shown that diameters of newly-formed particles should be larger  
567 than 70 nm to contribute to cloud condensation nuclei significantly (Man et al., 2015; Ma et  
568 al., 2021) and will be considered as haze particles when their size reaches larger than 100 nm  
569 (Kulmala et al., 2021). In Fig-[ure 12](#), we show ending diameters (End Dp) of newly formed  
570 grown particles during our observations at both sites. End Dp during the observation from  
571 June 14 to July 14 at UB site (21-105 nm, with a median of 49 nm, Fig-[ure 12a](#)) had similar  
572 characteristics as those during the long-term observation in summer (21-126 nm, with a  
573 median of 56 nm, Fig-[ure 12a](#)) where most of End Dp were in the range of 25-70 nm. As  
574 shown in Fig.12b, 61% of End Dp were in the range of 25-70 nm, and only 9% of End Dp  
575 were larger than 100 nm during our observation in summer 2018 and 2019 at UB site. We  
576 found that the ending diameters slightly higher at UB site than MT site, but the difference is  
577 not significant (49 nm vs 45 nm) as shown in [Figure-R\\_12c](#).

578 Earlier research has pointed out that in order to observe particle growth until 100 nm at a  
579 measurement station under typical conditions, simultaneous NPF should happen over a very  
580 large area (e.g. with wind speed 5 m/s and growth rate of 3 nm/h from the station to roughly  
581 600 km upwind from the station) (Paasonen et al., 2018). During our observation in summer  
582 2018 and 2019, most of the newly formed modes kept growing for about 20 hours after an  
583 NPF event started, and the maximum horizontal extension of the observed NPF events in the  
584 growth stage is restricted to within about 200 km (~2° in latitude) north of UB site (Fig-[ure](#)  
585 13). As shown in Fig-[ure 13](#), the population density is also higher within the area extending  
586 ~200 km north than beyond this limit. Therefore, it seems that NPF events were limited to the

587 regions with some contribution from anthropogenic emissions during air mass transport from  
588 north to Beijing. Roughly similar extent of the NPF area is also seen in other directions.  
589 However, towards the south it is more likely that increasing condensation sink from  
590 accumulating pollution becomes the limiting factor for NPF occurrence rather than  
591 decreasing strength in emission sources. NPF events at MT station had similar characteristics  
592 as those at UB station with the NPF event region extending a few hundred kilometers towards  
593 the north. The NPF events in this direction were disrupted after a relatively similar distance  
594 (or they enter the growth stagnation phase, ~~which will be discussed in section 3.6.3~~). The  
595 limited NPF event area could possibly explain why most End Dp we observed were smaller  
596 than 70 nm.

### 597 *3.5 Effect of topography*

598 In Figure 14, we show average particle number size distributions and particle number  
599 concentrations on NPF event and non-event days during our short-term parallel observation at  
600 both sites. On NPF event days, nucleation (6-25 nm) and Aitken (25-100 nm) mode particle  
601 number concentrations were much smaller at MT station than those at UB station due to  
602 smaller particle-formation rates and less anthropogenic emissions. Interestingly, accumulation  
603 (100-840 nm) mode particle number concentrations were higher at MT station (701-2900  
604  $\text{cm}^{-3}$ , with a median of  $1500 \text{ cm}^{-3}$ ) than ~~that those~~ at UB station (350-1416  $\text{cm}^{-3}$  with a median  
605 of  $700 \text{ cm}^{-3}$ ) (Figure 14b). Due to the close proximity of the two measurement sites, the air  
606 mass arrival directions and source regions were (mostly) similar at both sites throughout the  
607 measurement period, hence the regional and transported air masses cannot explain the higher  
608 accumulation mode particle number concentration at MT site. As there were few primary  
609 emissions at MT site, the accumulation mode particles could be attributed to secondary  
610 particles (Kulmala et al., 2021), indicating particles at MT station were more aged than those  
611 at UB station (Figure 14a). The possible reasons is that mountains block pollution diffusion,  
612 which in the end resulted in comparable CS at MT station as UB station.

613 Figure 15 shows an example of the wind distribution before and during NPF event on June

614 30, 2019 at 850 hPa (close to the altitude of MT station) and 10 m above ground level. As  
615 shown in Figure 15, the reanalyzed wind directions at 850 hPa were similar as those at 10 m  
616 above the ground level at MT station. Actually, the wind conditions on other NPF event days  
617 at MT station during our observation had similar characteristics that the wind directions were  
618 similar between 850 hPa and 10 m above ground level indicating air masses well mixed  
619 during NPF events. Earlier observations also found NPF event happened uniformly within the  
620 mixing layer at their observation stations and particle number size distribution remains  
621 roughly constant within the mixing layer (Shen et al., 2018; Lampilahti et al., 2021).

### 622 *3.6 case studies*

#### 623 *3.6.1 Non-local NPF events at MT station*

624 ~~As we discussed above, NPF events at MT stations were favored by strong photochemistry~~  
625 ~~(sufficient solar radiation) and low CS. However, we also observed two NPF events under~~  
626 ~~low solar radiation and high CS on June 15 and 25. These two NPF events had similar~~  
627 ~~characteristics, and we explain the case on June 15 in detail. During this case, air masses~~  
628 ~~arrived at both stations from south-east around 9:00 LT as shown in Fig. 16b&d, resulting in~~  
629 ~~high CS especially at MT and UB stations (Fig. 16a&e). The NPF event at the UB station was~~  
630 ~~observed around 11:00 LT, with a high median  $J_z$  of  $5.56 \text{ cm}^{-2} \text{ s}^{-1}$ , whereas no indication of~~  
631 ~~NPF event at MT was observed until 15:00 likely due to the high CS. After 15:00 LT, a new~~  
632 ~~growing mode from 15 nm appeared at MT station. Because there was no intense increase of~~  
633 ~~sub-15 nm particle number concentration throughout the whole event, the NPF event at MT~~  
634 ~~station was not local but occurred somewhere else and transported to MT station. This is a~~  
635 ~~common phenomenon, particularly when the conditions do not favor NPF events to occur on~~  
636 ~~site, but are NPF favorable somewhere else. The particles formed off site are transported~~  
637 ~~vertically or horizontally and observed on site (Dada et al., 2018; Leino et al., 2019).~~  
638 ~~Different from other NPF events, this non-local NPF event was associated with strong~~  
639 ~~southerly wind (Fig. 16e), the NPF event observed at the MT station might originate from~~  
640 ~~urban areas 60 km south to the station as shown in Fig.1, assuming the NPF event started~~



641 around 9:00 and the mean wind speed was 3 m/s.—

### 642 *3.6.2 Undefined day under low CS and high UV at MT station*

643 Interestingly, we also observed an undefined day at MT station with low CS ( $0.006 \text{ s}^{-1}$ ) and  
644 high UV ( $28 \text{ W/m}^2$ ) on June 28 (Fig. 17c) as there seems to be a very weak ‘banana’ around  
645 13:00 in the particle number size distribution plot. All other days with such conditions were  
646 classified as NPF event days. In this case, the reasonable explanation would be low precursor  
647 vapours which we think are  $\text{SO}_2$  in our case. On this day, an air mass from Inner Mongolia  
648 arrived at both stations, resulting in very low  $\text{SO}_2$  concentration at the UB station among all  
649 NPF event days during our observation as shown in Fig. 4. It is reasonable to assume that the  
650  $\text{SO}_2$  concentration was even lower at the MT station than at the UB station, and low  $\text{H}_2\text{SO}_4$   
651 concentration could also be expected, which could be insufficient to trigger an NPF event.  
652 This is consistent with an earlier long term observation at Shangdianzi, another background  
653 site of Beijing, where the NPF events were suppressed by air masses from Inner Mongolia  
654 due to the low precursor concentrations (Shen et al., 2018). In comparison, we observed a  
655 very weak NPF event at UB station at the same day, as local emissions were enough to supply  
656 enough vapors to initiate NPF event.

### 657 *3.6.3 I Growth stagnant and shrinkage case during our observation*

658 During our observations in summer 2018 and 2019 at urban site and the observation from  
659 June 14 to July 14, 2019 at MT site, there were some cases where the newly formed particles  
660 entered a phase of growth stagnation or even displayed a decreasing mode diameter. On June  
661 30, 2019 such case occurred simultaneously at both sites and we chose this day for a case  
662 study.

663 As shown in Fig.18 a&b, the newly formed particles entered a phase of growth stagnation  
664 almost at the same time around 12:00 at both sites. Particle mode diameters decreased from  
665 31 nm to 15 nm at UB station around 15:00, under relatively calm meteorological condition  
666 indicating meteorological condition could not be the reason for particle sizes decrease on  
667 June 30, 2019 at UB site. Around the same time, mode diameter at MT station also decreased  
668 gradually from 25 nm to 16 nm. Earlier observations in summer time Beijing have speculated

669 ~~mode diameter decrease to be related to particle evaporation, which is triggered by favorable~~  
670 ~~meteorological conditions and vapor dilution (Zhang et al., 2016). From Fig.13, we see, that~~  
671 ~~the air masses observed during the growth stagnation or diameter decrease (both marked~~  
672 ~~under growth stagnation in the figure) were often located quite far in the north over the less~~  
673 ~~populated areas during the onset time of regional NPF. It is also possible, that the less~~  
674 ~~favorable initial conditions for particle formation and growth over these areas, combined with~~  
675 ~~increasing wind speed or temporal changes in the growth rate, could explain the observations~~  
676 ~~of decreasing particle sizes without evaporation (Kivekäs et al., 2016; Hakala et al., 2019).~~

#### 677 4 Summary and conclusions

678 We conducted observations of NPF events at an urban site (UB) and a background mountain  
679 site (MT) in Beijing and fully analyzed the favorable conditions for NPF event occurrences at  
680 each of the sites. In order to identify the similarities and differences between NPF events at  
681 both stations in terms of frequency, intensity ~~and mechanisms~~, we compared certain NPF  
682 events' characteristics including ~~particle~~ formation rate, growth rate as well as NPF event  
683 start time and ending diameters of newly-formed growing particles at both stations. We found  
684 that NPF events are most of the time a regional phenomenon occurring over the studied areas  
685 and connected closely with air masses source regions during our observation. The air masses  
686 from north favored common NPF events more than any other mass trajectories due to their  
687 associated clean air masses and thus low CS. Additionally, air masses from the north group  
688 always resulted in an NPF event at UB station, while other factors still suppressed their  
689 occurrence at the MT station. For example, we found that sufficiently high solar radiation, e.g.  
690 UV (UVA+UVB) intensity larger than 15 W/m<sup>2</sup> is required for an NPF event to occur at MT  
691 and NPF events observed under solar radiation conditions smaller than 15 W/m<sup>2</sup> were rather  
692 transported NPF events from areas upwind to MT station. ~~Another factor suppressing the~~  
693 ~~occurrence of NPF events at MT is the too low precursor gas concentrations (e.g. SO<sub>2</sub>) which~~  
694 ~~was visible in MT rather than at UB.~~—Moreover, we found that the CS limit for NPF event  
695 occurrence at UB station was ~0.032 s<sup>-1</sup>, which is consistent with earlier observations in  
696 urban Beijing. In comparison, at MT station the CS limit ~~(assuming RH as 0% when~~

697 ~~calculating CS~~) could be ~~only~~  $\sim 0.013 \text{ s}^{-1}$ , above which local-NPF events could possibly be  
698 suppressed associated with the lower  $\text{SO}_2$  concentration.

699 Although NPF events could happen simultaneously at both stations, the NPF event strength  
700 (~~particle~~ formation rates) was significantly higher at UB than MT station, possibly due to  
701 spatial inhomogeneity in the sources of aerosol precursor compounds as well as solar  
702 radiation. In addition, the ~~particle~~ growth rates in size range of 7-15 nm were also slightly  
703 higher at UB than MT station. Regional NPF events were observed to occur with the  
704 horizontal extent within around 200 kilometers when air masses arriving at Beijing from the  
705 north, as a result, only a few NPF events were observed to end with mode diameters larger  
706 than 70 nm. The upwind extension of regional NPF events was limited to the areas with some  
707 anthropogenic emissions. There should not be any discrete boundary between the regions that  
708 NPF event is or is not occurring, but with decreasing anthropogenic emissions, the strength  
709 (formation rates and growth rates) should decrease. The size of the area with NPF events  
710 upwind our observation seems to be connected with population density that weaker NPF  
711 event was assumed to happen in less populated areas.

712 Overall, our results highlight the importance of anthropogenic emissions for NPF events  
713 occurrence and subsequently growth in north China plain during summer. However, there are  
714 still some uncertainties due to the limited data set. For more robust knowledge on NPF events  
715 in north China plain, and to figure out the effect of urban emissions on regional NPF events,  
716 we still need long-term observation including particle number size distribution down to sub-3  
717 nm, gas and particle phase chemistry long term and more comprehensive observations on  
718 NPF events upwind and downwind urban Beijing are important. Such observations can shed  
719 light into the regionality of NPF events and the dynamical development of the aerosol  
720 population influenced by radical chemistry in the plume of a megacity.

721 **Conflict of interest:** The authors declare no competing interests.

722 **Author contributions:** YZ, CY, YG, XY performed the measurements. YZ, SH, CY, YG, LD,  
723 XY analyzed the data. YZ, CY, SH, LD wrote the manuscript. All authors reviewed the paper  
724 and contributed to the scientific discussions.

725 **Data availability:** The data displayed in this manuscript will be available online at  
726 [zenodo.com](https://zenodo.com) once the manuscript is in its final publication format.

727 **Financial support:** This publication has been produced within the framework of the  
728 EMME-CARE project, which has received funding from the European Union’s Horizon 2020  
729 Research and Innovation Programme (under grant agreement no. 856612) and the  
730 Government of Cyprus. This research has also received funding from the European  
731 Commission grant agreement no. 742206 (“ERC-ATM-GTP”) as well as Academy of Finland  
732 Projects 316114 & 311932. Simo Hakala acknowledges the doctoral programme in  
733 Atmospheric Sciences (ATM-DP, University of Helsinki) for financial support. The sole  
734 responsibility of this publication lies with the author. The European Union is not responsible  
735 for any use that may be made of the information contained therein.

736

737

738 **5 References**

739 [Boulon, J., Sellegri, K., Hervo, M., Picard, D., Pichon, J.-M., Fréville, P., and Laj, P.:](#)  
740 [Investigation of nucleation events vertical extent: a long term study at two different altitude](#)  
741 [sites, \*Atmos. Chem. Phys.\*, 11, 5625–5639, <https://doi.org/10.5194/acp-11-5625-2011>, 2011.](#)

742 Cai, R., and Jiang, J.: A new balance formula to estimate new particle formation rate: reevaluating the  
743 effect of coagulation scavenging, *Atmos Chem Phys*, 17, 12659-12675, 10.5194/acp-17-12659-2017,  
744 2017.

745 Cai, R., Yang, D., Fu, Y., Wang, X., Li, X., Ma, Y., Hao, J., Zheng, J., and Jiang, J.: Aerosol surface  
746 area concentration: a governing factor in new particle formation in Beijing, *Atmos Chem Phys*, 17,  
747 12327-12340, 10.5194/acp-17-12327-2017, 2017.

748 Cai, R., Yan, C., Yang, D., Yin, R., Lu, Y., Deng, C., Fu, Y., Ruan, J., Li, X., Kontkanen, J., Zhang, Q.,  
749 Kangasluoma, J., Ma, Y., Hao, J., Worsnop, D. R., Bianchi, F., Paasonen, P., Kerminen, V.-M., Liu, Y.,  
750 Wang, L., Zheng, J., Kulmala, M., and Jiang, J.: Sulfuric acid-amine nucleation in urban Beijing,  
751 *Atmospheric Chemistry and Physics Discussions*, 10.5194/acp-2020-1060, 2020.

752 Carnerero, C., Pérez, N., Reche, C., Ealo, M., Titos, G., Lee, H.-K., Eun, H.-R., Park, Y.-H., Dada, L.,  
753 Paasonen, P., Kerminen, V.-M., Mantilla, E., Escudero, M., Gómez-Moreno, F. J., Alonso-Blanco, E.,  
754 Coz, E., Saiz-Lopez, A., Temime-Roussel, B., Marchand, N., Beddows, D. C. S., Harrison, R. M.,  
755 Petäjä, T., Kulmala, M., Ahn, K.-H., Alastuey, A., and Querol, X.: Vertical and horizontal distribution  
756 of regional new particle formation events in Madrid, *Atmos Chem Phys*, 18, 16601-16618,  
757 10.5194/acp-18-16601-2018, 2018.

758 [Casquero-Vera, J. A., Lyamani, H., Dada, L., Hakala, S., Paasonen, P., Román, R., Fraile, R.,](#)  
759 [Petäjä, T., Olmo-Reyes, F. J., and Alados-Arboledas, L.: New particle formation at urban and](#)  
760 [high-altitude remote sites in the south-eastern Iberian Peninsula, \*Atmos. Chem. Phys.\*, 20,](#)  
761 [14253–14271, <https://doi.org/10.5194/acp-20-14253-2020>, 2020.](#)

762 Chu, B., Dada, L., Liu, Y., Yao, L., Wang, Y., Du, W., Cai, J., Daellenbach, K., Chen, X., Simonen, P.,  
763 Zhou, Y., Deng, C., Fu, Y., Yin, R., Li, H., He, X.-C., Feng, Z., Yan, C., Kangasluoma, J., and Kulmala,  
764 M.: Particle growth with photochemical age from new particle formation to haze in the winter of

765 Beijing, China, *Science of The Total Environment.*, 753, 10.1016/j.scitotenv.2020.142207, 2021.

766 Chu, B. W., Kerminen, V. M., Bianchi, F., Yan, C., Petäjä, T., and Kulmala, M.: Atmospheric new  
767 particle formation in China, *Atmos Chem Phys*, 19, 115-138, <https://doi.org/10.5194/acp-19-115-2019>,  
768 2019.

769 Dada, L., Paasonen, P., Nieminen, T., Buenrostro Mazon, S., Kontkanen, J., Peräkylä, O., Lehtipalo,  
770 K., Hussein, T., Petäjä, T., Kerminen, V.-M., Bäck, J., and Kulmala, M.: Long-term analysis of  
771 clear-sky new particle formation events and nonevents in Hyytiälä, *Atmos Chem Phys*, 17, 6227-6241,  
772 10.5194/acp-17-6227-2017, 2017.

773 Dada, L., Chellapermal, R., Buenrostro Mazon, S., Paasonen, P., Lampilahti, J., Manninen, H. E.,  
774 Junninen, H., Petäjä, T., Kerminen, V.-M., and Kulmala, M.: Refined classification and  
775 characterization of atmospheric new-particle formation events using air ions, *Atmos Chem Phys*, 18,  
776 17883-17893, 10.5194/acp-18-17883-2018, 2018.

777 Dada, L., Lehtipalo, K., Kontkanen, J., Nieminen, T., Baalbaki, R., Ahonen, L., Duplissy, J., Yan, C.,  
778 Chu, B., Petäjä, T., Lehtinen, K., Kerminen, V.-M., Kulmala, M., and Kangasluoma, J.: Formation and  
779 growth of sub-3-nm aerosol particles in experimental chambers, *Nat Protoc.*, 15, 1013-1040,  
780 10.1038/s41596-019-0274-z, 2020a.

781 Dada, L., Ylivinkka, I., Baalbaki, R., Li, C., Guo, Y., Yan, C., Yao, L., Sarnela, N., Jokinen, T.,  
782 Daellenbach, K. R., Yin, R., Deng, C., Chu, B., Nieminen, T., Kontkanen, J., Stolzenburg, D., Sipilä,  
783 M., Hussein, T., Paasonen, P., Bianchi, F., Salma, I., Weidinger, T., Pikridas, M., Sciare, J., Jiang, J.,  
784 Liu, Y., Petäjä, T., Kerminen, V.-M., and Kulmala, M.: Sources and sinks driving sulphuric acid  
785 concentrations in contrasting environments: implications on proxy calculations, *Atmos. Chem. Phys.*  
786 *Discuss.*, 10.5194/acp-2020-155, 2020b.

787 Dai, L., Wang, H., Zhou, L., An, J., Tang, L., Lu, C., Yan, W., Liu, R., Kong, S., Chen, M., Lee, S.,  
788 and Yu, H.: Regional and local new particle formation events observed in the Yangtze River Delta  
789 region, China, *Journal of Geophysical Research: Atmospheres*, 122, 2389-2402,  
790 10.1002/2016jd026030, 2017.

791 Dal Maso, M., Kulmala, M., Riipinen, I., Wagner, R., Hussein, T., Aalto, P. P., and Lehtinen, K. E. J.:  
792 Formation and growth of fresh atmospheric aerosols: eight years of aerosol size distribution data from

793 SMEAR II, Hyytiälä, Finland, *Boreal Environ Res*, 10, 323-336, 2005.

794 Deng, C., Cai, R., Yan, C., Zheng, J., and Jiang, J.: Formation and growth of sub-3 nm particles in  
795 megacities: impact of background aerosols, *Faraday Discuss*, 10.1039/d0fd00083c, 2020a.

796 Deng, C., Fu, Y., Dada, L., Yan, C., Cai, R., Yang, D., Zhou, Y., Yin, R., Lu, Y., Li, X., Qiao, X., Fan,  
797 X., Nie, W., Kontkanen, J., Kangasluoma, J., Chu, B., Ding, A., Kerminen, V. M., Paasonen, P.,  
798 Worsnop, D. R., Bianchi, F., Liu, Y., Zheng, J., Wang, L., Kulmala, M., and Jiang, J.: Seasonal  
799 Characteristics of New Particle Formation and Growth in Urban Beijing, *Environ Sci Technol*, 54,  
800 8547-8557, 10.1021/acs.est.0c00808, 2020b.

801 Du, W., Dada, L., Zhao, J., Chen, X., Daellenbach, K. R., Xie, C., Wang, W., He, Y., Cai, J., Yao, L.,  
802 Zhang, Y., Wang, Q., Xu, W., Wang, Y., Tang, G., Cheng, X., Kokkonen, T. V., Zhou, W., Yan, C., Chu,  
803 B., Zha, Q., Hakala, S., Kurppa, M., Järvi, L., Liu, Y., Li, Z., Ge, M., Fu, P., Nie, W., Bianchi, F.,  
804 Petäjä, T., Paasonen, P., Wang, Z., Worsnop, D. R., Kerminen, V.-M., Kulmala, M., and Sun, Y.: A 3D  
805 study on the amplification of regional haze and particle growth by local emissions, *npj Climate and  
806 Atmospheric Science*, 4, 10.1038/s41612-020-00156-5, 2021.

807 Ehn, M., Thornton, J.A., Kleist, E., Sipila, M., Junninen, H., Pullinen, I., Springer, M., Rubach, F.,  
808 Tillmann, R., Lee, B., Lopez-Hilfiker, F., Andres, S., Acir, I.-H., Rissanen, M., Jokinen, T.,  
809 Schobesberger, S., Kangasluoma, J., Kontkanen, J., Nieminen, T., Kurten, T., Nielsen, L. B.,  
810 Jorgensen, S., Kjaergaard, H. G., Canagaratna, M., Maso, M. D., Berndt, T., Petaja, T., Wahner, A.,  
811 Kerminen, V.-M., Kulmala, M., Worsnop, D. R., Wildt, J., and Mentel, T. F.: A large source of  
812 low-volatility secondary organic aerosol, *Nature*, 506, 476–479., 2014.

813 Gao, Y., Zhang, D., Wang, J., Gao, H., and Yao, X.: Variations in Ncn and Nccn over China marginal  
814 seas related to marine traffic emissions, new particle formation and aerosol aging, *Atmos. Chem.  
815 Phys.*, in press 2020.

816 Guo, S., Hu, M., Zamora, M. L., Peng, J. F., Shang, D. J., Zheng, J., Du, Z. F., Wu, Z., Shao, M., Zeng,  
817 L. M., Molina, M. J., and Zhang, R. Y.: Elucidating severe urban haze formation in China, *P Natl  
818 Acad Sci USA*, 111, 17373-17378, 10.1073/pnas.1419604111, 2014.

819 Guo, S., Hu, M., Peng, J., Wu, Z., Zamora, M. L., Shang, D., Du, Z., Zheng, J., Fang, X., Tang, R.,  
820 Wu, Y., Zeng, L., Shuai, S., Zhang, W., Wang, Y., Ji, Y., Li, Y., Zhang, A. L., Wang, W., Zhang, F.,

821 Zhao, J., Gong, X., Wang, C., Molina, M. J., and Zhang, R.: Remarkable nucleation and growth of  
822 ultrafine particles from vehicular exhaust, *Proc Natl Acad Sci U S A*, 117, 3427-3432,  
823 10.1073/pnas.1916366117, 2020.

824 Hakala, S., Alghamdi, M. A., Paasonen, P., Vakkari, V., Khoder, M. I., Neitola, K., Dada, L.,  
825 Abdelmaksoud, A. S., Al-Jeelani, H., Shabbaj, I. I., Almeahmadi, F. M., Sundström, A.-M., Lihavainen,  
826 H., Kerminen, V.-M., Kontkanen, J., Kulmala, M., Hussein, T., and Hyvärinen, A.-P.: New particle  
827 formation, growth and apparent shrinkage at a rural background site in western Saudi Arabia, *Atmos*  
828 *Chem Phys*, 19, 19, <https://doi.org/10.5194/acp-19-10537-2019>, 2019.

829 Hamed, A., Korhonen, H., Sihto, S.-L., Joutsensaari, J., Järvinen, H., Petäjä, T., Arnold, F., Nieminen,  
830 T., Kulmala, M., Smith, J. N., Lehtinen, K. E. J., Laaksonen, A., and High relative humidity supresses  
831 continental new particle formation events, 2010.

832 Hamed, A., Korhonen, H., Sihto, S.-L., Joutsensaari, J., Järvinen, H., Petäjä, T., Arnold, F., Nieminen,  
833 T., Kulmala, M., Smith, J. N., Lehtinen, K. E. J., and Laaksonen, A.: The role of relative humidity in  
834 continental new particle formation, *Journal of Geophysical Research*, 116, 10.1029/2010jd014186,  
835 2011.

836 Herrmann, E., Ding, A. J., Kerminen, V. M., Petäjä, T., Yang, X. Q., Sun, J. N., Qi, X. M., Manninen,  
837 H., Hakala, J., Nieminen, T., Aalto, P. P., Kulmala, M., and Fu, C. B.: Aerosols and nucleation in  
838 eastern China: first insights from the new SORPES-NJU station, *Atmos Chem Phys*, 14, 2169-2183,  
839 10.5194/acp-14-2169-2014, 2014.

840 Hussein, T., Junninen, H., Tunved, P., Kristensson, A., Dal Maso, M., Riipinen, I., Aalto, P. P.,  
841 Hansson, H. C., Swietlicki, E., and Kulmala, M.: Time span and spatial scale of regional new particle  
842 formation events over Finland and Southern Sweden, *Atmos Chem Phys*, 9, 4699-4716,  
843 10.5194/acp-9-4699-2009, 2009.

844 Jun, Y.-S., Jeong, C.-H., Sabaliauskas, K., Richard Leitch, W., and Evans, G. J.: A year-long  
845 comparison of particle formation events at paired urban and rural locations, *Atmospheric Pollution*  
846 *Research*, 5, 447-454, 10.5094/apr.2014.052, 2014.

847 Kangasluoma, J., Cai, R., Jiang, J., Deng, C., Stolzenburg, D., Ahonen, L. R., Chan, T., Fu, Y., Kim,  
848 C., Laurila, T. M., Zhou, Y., Dada, L., Sulo, J., Flagan, R. C., Kulmala, M., Petäjä, T., and Lehtipalo,



849 K.: Overview of measurements and current instrumentation for 1–10 nm aerosol particle number size  
850 distributions, *J Aerosol Sci*, 148, 10.1016/j.jaerosci.2020.105584, 2020.

851 Kerminen, V. M., Chen, X. M., Vakkari, V., Petäjä, T., Kulmala, M., and Bianchi, F.: Atmospheric new  
852 particle formation and growth: review of field observations, *Environ Res Lett*, 13,  
853 <https://doi.org/10.1088/1748-9326/aadf3c>, 2018.

854 [Komppula, M., Lihavainen, H., Hatakka, J., Paatero, J., Aalto, P., Kulmala, M., and Viisanen,](#)  
855 [Y.: Observations of new particle formation and size distributions at two different heights and](#)  
856 [surroundings in subarctic area in northern Finland, \*J. Geophys. Res.-Atmos.\*, 108, 4295,](#)  
857 [<https://doi.org/10.1029/2002jd002939>, 2003.](#)

858 Komppula, M., Sihto, S.-L., Korhonen, H., Lihavainen, H., Kerminen, V.-M., Kulmala, M., and  
859 Viisanen, Y.: New particle formation in air mass transported between two measurement sites in  
860 Northern Finland, *Atmos Chem Phys*, 6, 14, [www.atmos-chem-phys.net/6/2811/2006/](http://www.atmos-chem-phys.net/6/2811/2006/), 2006.

861 Kontkanen, J., Deng, C., and Fu, Y., Dada, L., Zhou, Y., Cai, J., Daellenbach, R.-K., Hakala, S.,  
862 Kokkonen, V.-T., Lin, Z., Liu, Y., Wang, Y., Yan, C., Petäjä, T., Jiang, J., Kulmala, M and Paasonen, P.:  
863 Size-resolved particle number emissions in Beijing determined from measured particle size  
864 distributions, *Atmos Chem Phys*, 20, 11329–11348, <https://doi.org/10.5194/acp-20-11329-2020>, 2020.

865 Kivekäs, N., Carpman, J., Roldin, P., Leppä, J., O'Connor, E., Kristensson, A., and Asmi, E.:  
866 Coupling an aerosol box model with one-dimensional flow: a tool for understanding  
867 observations of new particle formation events, *Tellus B*, 68, 29706,  
868 [doi:10.3402/tellusb.v68.29706](https://doi.org/10.3402/tellusb.v68.29706), 2016.

869 Kristensson, A., Johansson, M., Swietlicki, E., Kivekäs, N., Hussein, T., Nieminen, T., Kulmala, M.,  
870 and Dal Maso, M.: NanoMap: geographical mapping of atmospheric new particle formation through  
871 analysis of particle number size distribution data, *Boreal Environ. Res.*, 19 (suppl. B), 329–342,  
872 2014.

873 Kulmala, M., Petäjä, T., Nieminen, T., Sipilä, M., Manninen, H. E., Lehtipalo, K., Dal Maso, M.,  
874 Aalto, P. P., Junninen, H., Paasonen, P., Riipinen, I., Lehtinen, K. E. J., Laaksonen, A., and Kerminen,  
875 V. M.: Measurement of the nucleation of atmospheric aerosol particles, *Nat Protoc*, 7, 1651-1667,  
876 <https://doi.org/10.1038/nprot.2012.091>, 2012.

877 Kulmala, M., Dada, L., Dällenbach, K., Yan, C., Stolzenburg, D., Kontkanen, J., Ezhova, E., Hakala,  
878 S., Tuovinen, S., Kokkonen, T., Kurppa, M., Cai, R., Zhou, Y., Yin, R., Baalbaki, R., Chan, T., Chu, B.,  
879 Deng, C., Fu, Y., Ge, M., He, H., Heikkinen, L., Junninen, H., Nei, W., Rusanen, A., Vakkari, V.,  
880 Wang, Y., Wang, L., yao, I., Zheng, J., Kujansuu, J., Kangasluoma, J., Petäjä, T., Paasonen, P., Järvi,  
881 L., Worsnop, D., Ding, A., Liu, Y., Jiang, J., Bianchi, F., Yang, G., Liu, Y., Lu, Y., and Kerminen,  
882 V.-M.: Is reducing new particle formation a plausible solution to mitigate particulate air pollution in  
883 Beijing and other Chinese megacities?, *Faraday Discuss*, 10.1039/d0fd00078g, 2021.

884 Lampilahti, J., Manninen, H. E., Nieminen, T., Mirme, S., Ehn, M., Pullinen, I., Leino, K.,  
885 Schobesberger, S., Kangasluoma, J., Kontkanen, J., Järvinen, E., Väänänen, R., Yli-Juuti, T., Krejci,  
886 R., Lehtipalo, K., Levula, J., Mirme, A., Decesari, S., Tillmann, R., Worsnop, D. R., Rohrer, F.,  
887 Kiendler-Scharr, A., Petäjä, T., Kerminen, V.-M., Mentel, T. F., and Kulmala, M.: Zeppelin-led study  
888 on the onset of new particle formation in the planetary boundary layer, *Atmospheric Chemistry and*  
889 *Physics Discussions*, 10.5194/acp-2021-282, 2021.

890 Lehtipalo, K., Leppä, J., Kontkanen, J., Kangasluoma, J., Wimmer, D., Franchin, A., Schobesberger,  
891 S., Junninen, H., Petäjä, T., Sipilä, M., Mikkilä, J., Vanhanen, J., Worsnop, D. r., and Kulmala, M.:  
892 methods for determining particle size distribution and growth rates between 1 and 3 nm using the  
893 Particle Size Magnifier, *Boreal Environ Res*, 19 215-236, 2014.

894 Lehtipalo, K., Yan, C., Dada, L., Bianchi, F., Xiao, M., Wagner, R., Stolzenburg, D., Ahonen, L. R.,  
895 Amorim, A., Baccarini, A., Bauer, P. S., Baumgartner, B., Bergen, A., Bernhammer, A. K.,  
896 Breitenlechner, M., Brilke, S., Buchholz, A., Mazon, S. B., Chen, D. X., Chen, X. M., Dias, A.,  
897 Dommen, J., Draper, D. C., Duplissy, J., Ehn, M., Finkenzeller, H., Fischer, L., Frege, C., Fuchs, C.,  
898 Garmash, O., Gordon, H., Hakala, J., He, X. C., Heikkinen, L., Heinritzi, M., Helm, J. C., Hofbauer,  
899 V., Hoyle, C. R., Jokinen, T., Kangasluoma, J., Kerminen, V. M., Kim, C., Kirkby, J., Kontkanen, J.,  
900 Kurten, A., Lawler, M. J., Mai, H. J., Mathot, S., Mauldin, R. L., Molteni, U., Nichman, L., Nie, W.,  
901 Nieminen, T., Ojdanic, A., Onnela, A., Passananti, M., Petäjä, T., Piel, F., Pospisilova, V., Quéléver, L.  
902 L. J., Rissanen, M. P., Rose, C., Sarnela, N., Schallhart, S., Schuchmann, S., Sengupta, K., Simon, M.,  
903 Sipilä, M., Tauber, C., Tomé, A., Tröstl, J., Väisänen, O., Vogel, A. L., Volkamer, R., Wagner, A. C.,  
904 Wang, M. Y., Weitz, L., Wimmer, D., Ye, P. L., Ylisirnio, A., Zha, Q. Z., Carslaw, K. S., Curtius, J.,

905 Donahue, N. M., Flagan, R. C., Hansel, A., Riipinen, I., Virtanen, A., Winkler, P. M., Baltensperger,  
906 U., Kulmala, M., and Worsnop, D. R.: Multicomponent new particle formation from sulfuric acid,  
907 ammonia, and biogenic vapors, *Sci Adv*, 4, <https://doi.org/10.1126/sciadv.aau5363>, 2018.

908 Leino, K., Lampilahti, J., Poutanen, P., Väänänen, R., Manninen, A., Buenrostro Mazon, S., Dada, L.,  
909 Franck, A., Wimmer, D., Aalto, P. P., Ahonen, L. R., Enroth, J., Kangasluoma, J., Keronen, P.,  
910 Korhonen, F., Laakso, H., Matilainen, T., Siivola, E., Manninen, H. E., Lehtipalo, K., Kerminen,  
911 V.-M., Petäjä, T., and Kulmala, M.: Vertical profiles of sub-3&thinsp;nm particles over the boreal  
912 forest, *Atmos Chem Phys*, 19, 4127-4138, [10.5194/acp-19-4127-2019](https://doi.org/10.5194/acp-19-4127-2019), 2019.

913 Liu, J., Zhang, X. L., Xu, X. F., and Xu, H. H.: Comparison analysis of variation characteristics of  
914 SO<sub>2</sub>, NO<sub>x</sub>, O<sub>3</sub> and PM<sub>2.5</sub> between rural and urban areas, *Beijing Huan jing ke xue= Huanjing kexue*  
915 / [bian ji, Zhongguo ke xue yuan huan jing ke xue wei yuan hui "Huan jing ke xue" bian ji wei yuan  
916 hui.], 29, 1059-1065, 2008.

917 Liu, J. Q., Jiang, J. K., Zhang, Q., Deng, J. G., and Hao, J. M.: A spectrometer for measuring particle  
918 size distributions in the range of 3 nm to 10 μm, *Front Env Sci Eng*, 10, 63-72,  
919 <https://doi.org/10.1007/s11783-014-0754-x>, 2016.

920 Lee, B. P., Li, Y. J., Flagan, R. C., Lo, C., and Chan, C. K.: Sizing characterization of the fast mobility  
921 particle sizer (FMPS) against SMPS and HR-ToF-AMS, *Aerosol Sci. Technol.*, 47, 1030-1037,  
922 <https://doi.org/10.1080/02786826.2013.810809>, 2013.

923 Lu, Y., Yan, C., Fu, Y., Chen, Y., Liu, Y., Yang, G., Wang, Y., Bianchi, F., Chu, B., and Zhou, Y.: A  
924 proxy for atmospheric daytime gaseous sulfuric acid concentration in urban Beijing, *Atmos Chem*  
925 *Phys*, 19, 1971-1983, [10.5194/acp-19-1971-2019](https://doi.org/10.5194/acp-19-1971-2019), 2019.

926 Ma, L., Zhu, Y., Zheng, M., Sun, Y., Huang, L., Liu, X., Gao, Y., Shen, Y., Gao, H., and Yao, X.:  
927 Investigating three patterns of new particles growing to the size of cloud condensation nuclei in  
928 Beijing's urban atmosphere, *Atmos Chem Phys*, 21, 183-200, [10.5194/acp-21-183-2021](https://doi.org/10.5194/acp-21-183-2021), 2021.

929 Man, H. Y., Zhu, Y. J., Ji, F., Yao, X. H., Lau, N. T., Li, Y. J., Lee, B. P., and Chan, C. K.: Comparison  
930 of Daytime and Nighttime New Particle Growth at the HKUST Supersite in Hong Kong, *Environ Sci*  
931 *Technol*, 49, 7170-7178, 2015.

932 Olauson, J.: ERA5: The new champion of wind power modelling?, *Renewable Energy*, 126, 322-331,

933 2018.

934 Paasonen, P., Peltola, M., Kontkanen, J., Junninen, H., Kerminen, V.-M., and Kulmala, M.:  
935 Comprehensive analysis of particle growth rates from nucleation mode to cloud condensation nuclei  
936 in boreal forest, *Atmos Chem Phys*, 18, 12085-12103, 10.5194/acp-18-12085-2018, 2018.

937 Pierce, J. R., and Adams P. J.: Uncertainty in global CCN concentrations from uncertain  
938 aerosol nucleation and primary emission rates. *Atmos. Chem. Phys.*, 9,  
939 1339–1356, 10.5194/acp-9-1339-2009, 2009.

940 Qi, X., Ding, A., Roldin, P., Xu, Z., Zhou, P., Sarnela, N., Nie, W., Huang, X., Rusanen, A., Ehn, M.,  
941 Rissanen, M. P., Petäjä, T., Kulmala, M., and Boy, M.: Modelling studies of HOMs and their  
942 contributions to new particle formation and growth: comparison of boreal forest in Finland and a  
943 polluted environment in China, *Atmos Chem Phys*, 18, 11779-11791, 10.5194/acp-18-11779-2018,  
944 2018.

945 Qi, X. M. D., A. J., Nie, W., Petaja, T., Kerminen, V. M., Herrmann, E., Xie, Y. N., Zheng, L. F.,  
946 Manninen, H., Aalto, P., Sun, J. N., Xu, Z. N., Chi, X. G, Huang, X., Boy, M., Virkkula, A., Yang, X.  
947 Q., Fu, C. B., and Kulmala, M.: Aerosol size distribution and new particle formation in the western  
948 Yangtze River Delta of China: 2 years of measurements at the SORPES station, *Atmos Chem Phys*, 15,  
949 12445-12464, 2015.

950 Salma, I., Borsós, T., Weidinger, T., Aalto, P., Hussein, T., Dal Maso, M., and Kulmala, M.:  
951 Production, growth and properties of ultrafine atmospheric aerosol particles in an urban environment.  
952 *Atmospheric Chemistry and Physics*. 11. 10.5194/acp-11-1339-2011,2011.

953 Salma, I., Németh, Z., Kerminen, V.-M., Aalto, P., Nieminen, T., Weidinger, T., Molnár, Á., Imre, K.,  
954 and Kulmala, M.: Regional effect on urban atmospheric nucleation, *Atmos Chem Phys*, 16,  
955 8715-8728, 10.5194/acp-16-8715-2016, 2016.

956 [Sellegri, K., Rose, C., Marinoni, A., Lupi, A., Wiedensohler, A., Andrade, M., Bonasoni, P., and Laj,](#)  
957 [P.: New particle formation: A review of ground-based observations at mountain research stations.](#)  
958 [Atmosphere](#). 10. 493, <https://doi.org/10.3390/atmos10090493>, 2019.

959 Shen, X., Sun, J., Kivekäs, N., Kristensson, A., Zhang, X., Zhang, Y., Zhang, L., Fan, R., Qi, X., Ma,  
960 Q., and Zhou, H.: Spatial distribution and occurrence probability of regional new particle formation

961 events in eastern China, *Atmos Chem Phys*, 18, 587-599, 10.5194/acp-18-587-2018, 2018.

962 Shen, X. J., Sun, J. Y., Zhang, Y. M., Wehner, B., Nowak, A., Tuch, T., Zhang, X. C., Wang, T. T.,  
963 Zhou, H. G., Zhang, X. L., Dong, F., Birmili, W., and Wiedensohler, A.: First long-term study of  
964 particle number size distributions and new particle formation events of regional aerosol in the North  
965 China Plain, *Atmos Chem Phys*, 11, 1565-1580, 2011.

966 Stohl, A., Forster, C., Frank, A., Seibert, P., and Wotawa, G.: Technical note: The Lagrangian particle  
967 dispersion model FLEXPART version 6.2. , *Atmospheric Chemistry and Physics*, 5, 24,  
968 10.5194/acp-5-2461-2005., 2005.

969 Vana, M., Komsaare, K., Hörrak, U., Mirme, S., Nieminen, T., Petäjä, T., Noe, S. M., Kontkanen, J.,  
970 Manninen, H. E., , and Kulmala, M.: Characteristics of new-particle formation at three SMEAR  
971 stations, *Boreal Environ Res*, 21, 17, 2016.

972 Wang, J., Shen, Y., Li, K., Gao, Y., Gao, H., and Yao, X.: Nucleation-mode particle pool and large  
973 increases in Ncn and Ncn observed over the northwestern Pacific Ocean in the spring of 2014. ,  
974 *Atmos. Chem. Phys.*, 19, 17, <https://doi.org/10.5194/acp-19-8845-2019>, 2019.

975 Wang, M., Zhu, T., Zhang, J. P., Zhang, Q. H., Lin, W. W., Li, Y., and Wang, Z. F.: Using a mobile  
976 laboratory to characterize the distribution and transport of sulfur dioxide in and around Beijing, *Atmos*  
977 *Chem Phys*, 11, 11631-11645, 2011.

978 Wang, Z. B., Hu, M., Sun, J. Y., Wu, Z. J., Yue, D. L., Shen, X. J., Zhang, Y. M., Pei, X. Y., Cheng, Y.  
979 F., and Wiedensohler, A.: Characteristics of regional new particle formation in urban and regional  
980 background environments in the North China Plain, *Atmos Chem Phys*, 13, 12495-12506,  
981 10.5194/acp-13-12495-2013, 2013.

982 Wang, Z. B., Wu, Z. J., Yue, D. L., Shang, D. J., Guo, S., Sun, J. Y., Ding, A. J., Wang, L., Jiang, J. K.,  
983 Guo, H., Gao, J., Cheung, H. C., Morawska, L., Keywood, M., and Hu, M.: New particle formation in  
984 China: Current knowledge and further directions, *Science of the Total Environment*, 577, 258-266,  
985 2017.

986 Wu, Z., Hu, M., Liu, S., Wehner, B., Bauer, S., Maßling, A., Wiedensohler, A., Petäjä, T., Dal Maso,  
987 M., and Kulmala, M.: New particle formation in Beijing, China: Statistical analysis of a 1-year data  
988 set, *Journal of Geophysical Research*, 112, 10.1029/2006jd007406, 2007.

989 Yang-Chun, Y., Bo, H., and Wang, Y.: Changing Characteristics of the Main Air Pollutants of the  
990 Dongling Mountain in Beijing, *Environmental Science*, 34, 8, 2013.

991 Yao, L., Garmash, O., Bianchi, F., Zheng, J., Yan, C., Kontkanen, J., Junninen, H., Mazon, S. B., Ehn,  
992 M., Paasonen, P., Sipilä, M., Wang, M. Y., Wang, X. K., Xiao, S., Chen, H. F., Lu, Y. Q., Zhang, B. W.,  
993 Wang, D. F., Fu, Q. Y., Geng, F. H., Li, L., Wang, H. L., Qiao, L. P., Yang, X., Chen, J. M., Kerminen,  
994 V. M., Petäjä, T., Worsnop, D. R., Kulmala, M., and Wang, L.: Atmospheric new particle formation  
995 from sulfuric acid and amines in a Chinese megacity, *Science*, 361, 278-281,  
996 <https://doi.org/10.1126/science.aao4839>, 2018.

997 Yao, L., Fan, X., Yan, C., Kurtén, T., Daellenbach, K. R., Li, C., Wang, Y., Guo, Y., Dada, L., and  
998 Rissanen, M. P., Cai, J., Tham, Y. J., Zha, Q., Zhang, S., Du, W., Yu, M., Zheng, F., Zhou, Y.,  
999 Kontkanen, J., Chan, T., Shen, J., Kujansuu, J. T., Kangasluoma, J., Jiang, J., Wang, L., Worsnop, D.  
1000 R., Petäjä, T., Kerminen, V.-M., Liu, Y., Chu, B., He, H., Kulmala, M., and Bianchi, F.:  
1001 Unprecedented Ambient Sulfur Trioxide (SO<sub>3</sub>) Detection: Possible Formation Mechanism and  
1002 Atmospheric Implications, *Environ Sci Tech Let* 7, 809-818, [10.1021/acs.estlett.0c00615](https://doi.org/10.1021/acs.estlett.0c00615), 2020.

1003 Ying, G., Ma, J., and Xing, Y.: Comparison of air quality management strategies of PM<sub>10</sub>, SO<sub>2</sub>, and  
1004 NO<sub>x</sub> by an industrial source complex model in Beijing, *Environmental Progress*, 26, 33-42, 2010.

1005 Yu, F. and Luo, G.: Simulation of particle size distribution with a global aerosol model:  
1006 contribution of nucleation to aerosol and CCN number concentrations, *Atmos. Chem. Phys.*,  
1007 9, 7691–7710, [10.5194/acp-9-7691-2009](https://doi.org/10.5194/acp-9-7691-2009), 2009.

1008 Zhang, J., Chen, Z., Lu, Y., Gui, H., Liu, J., Wang, J., Yu, T., and Cheng, Y.: Observations of New  
1009 Particle Formation, Subsequent Growth and Shrinkage during Summertime in Beijing, *Aerosol Air  
1010 Qual Res*, 16, 1591-1602, [10.4209/aaqr.2015.07.0480](https://doi.org/10.4209/aaqr.2015.07.0480), 2016.

1011 Zhou, Y., Dada, L., Liu, Y., and Fu, Y., Kangasluoma, J., Chan, T., Yan, C., Chu, B., Daellenbach, K.  
1012 R., Bianchi, F., Kokkonen, T. V., Liu, Y., Kujansuu, J., Kerminen, V.-M., Petäjä, T., Wang, L., Jiang, J.,  
1013 and Kulmala, M.: Variation of size-segregated particle number concentrations in wintertime Beijing,  
1014 *Atmos Chem Phys*, 20, 1201-1216 [10.5194/acp-20-1201-2020](https://doi.org/10.5194/acp-20-1201-2020), 2020.

1015 Zimmerman, N., Jeong, C.-H., Wang, J. M., Ramos, M., Wallace, J. S., and Evans, G. J.: A  
1016 source-independent empirical correction procedure for the fast mobility and engine exhaust particle

1017 sizers, Atmos. Environ., 100, 7, 838 10.1016/j.atmosenv.2014.10.054, 2015., 2015.

1018

1019

1020

1021 Tables and Figures

1022 Table 1: NPF event and non- event days during our observation at both stations.

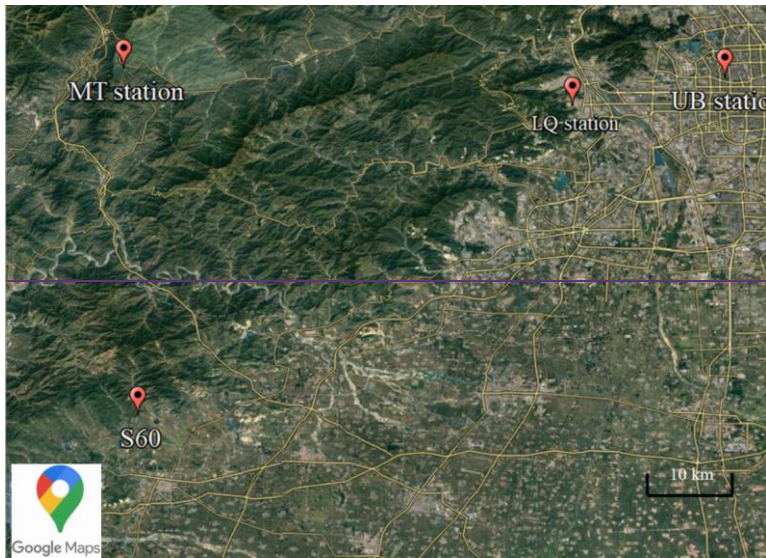
Date	Type	Air masses (9:00-15:00)		GR <sub>7-15nm</sub> (nm/h)		J <sub>7</sub> (cm <sup>-3</sup> s <sup>-1</sup> )		Event Start (LT)		Ending diameter (nm)		CS (s <sup>-1</sup> )	
		UB	MT	UB	MT	UB	MT	UB	MT	UB	MT	UB	MT
2019/06/14	a	North	North	8.61	-	4.97	-	9:00	8:00	71	-	<a href="#">0.017</a>	<a href="#">0.008</a>
2019/06/15*	a	Local	Local	12.63	-	5.56	-	11:00	15:00	82	60	<a href="#">0.013</a>	<a href="#">0.029</a>
2019/06/17	d	East	Local									<a href="#">0.031</a>	<a href="#">0.011</a>
2019/06/18	c	Local	West		10.5		0.17		12:00		45	<a href="#">0.039</a>	<a href="#">0.008</a>
2019/06/19	d	South	Local									<a href="#">0.037</a>	<a href="#">0.047</a>
2019/06/21	d	East	Local									<a href="#">0.035</a>	<a href="#">0.018</a>
2019/06/23	e	East	East									<a href="#">0.033</a>	<a href="#">0.013</a>
2019/06/24	f	Local	Local		8.21		-		12:00		50	<a href="#">0.027</a>	<a href="#">0.014</a>
2019/06/25*	a	Local	Local	-	-	-	-	12:00	15:00	-	53	<a href="#">0.032</a>	<a href="#">0.027</a>
2019/06/28	g	West	West	-		-		11:00				<a href="#">0.022</a>	<a href="#">0.006</a>
2019/06/29	a	North	North	12.93	7.14	6.93	2.28	9:00	8:00	21	19	<a href="#">0.008</a>	<a href="#">0.011</a>
2019/06/30	a	North	North	4.82	6.57	9.86	1.37	6:30	9:30	31	25	<a href="#">0.003</a>	<a href="#">0.008</a>
2019/07/01	a	North	North	7.31	5.82	3.84	0.82	9:00	8:30	105	102	<a href="#">0.006</a>	<a href="#">0.009</a>
2019/07/02	d	Local	West									<a href="#">0.013</a>	<a href="#">0.014</a>
2019/07/03	a	North	North	7.89	6.52	3.25	0.75	9:00	8:00	72	46	<a href="#">0.015</a>	<a href="#">0.006</a>
2019/07/04	b	Local	Local	-		-		10:00		53		<a href="#">0.012</a>	<a href="#">0.012</a>
2019/07/06	a	North	North	7.39	6.51	9.21	1.75	7:00	9:30	25	19	<a href="#">0.004</a>	<a href="#">0.011</a>
2019/07/07	b	North	North	7.61		3.61		9:00		32		<a href="#">0.008</a>	<a href="#">0.005</a>
2019/07/08	d	East	East									<a href="#">0.019</a>	<a href="#">0.012</a>
2019/07/09	d	East	East									<a href="#">0.021</a>	<a href="#">0.015</a>
2019/07/10	h	East	East									<a href="#">0.017</a>	<a href="#">0.013</a>
2019/07/11	d	East	East									<a href="#">0.039</a>	<a href="#">0.014</a>



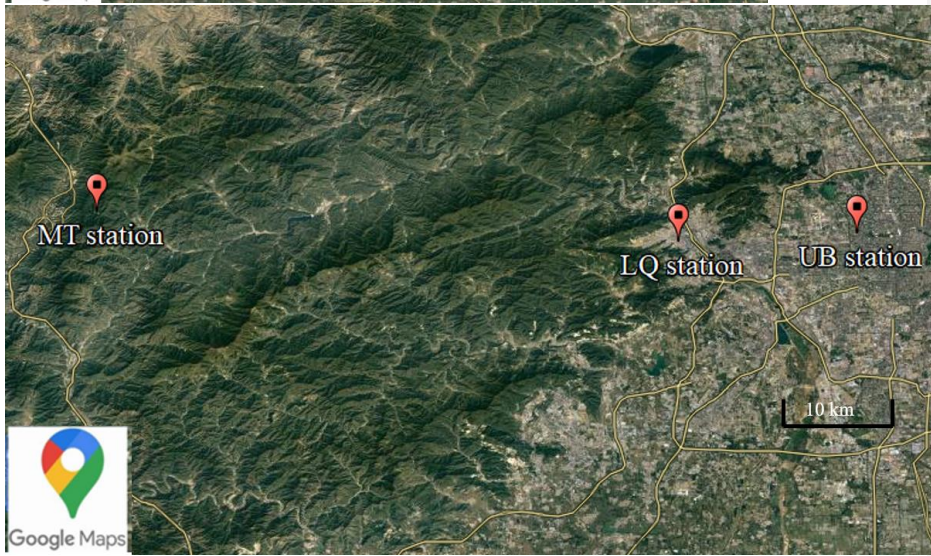
<b>2019/07/12</b>	f	East	East		5.57		0.37		9:30		24	<u>0.018</u>	<u>0.014</u>
<b>2019/07/13</b>	c	Local	North		6.32		0.70		10:00		30	<u>0.037</u>	<u>0.012</u>
<b>2019/07/14</b>	a	North	North	12.04	9.86	3.91	0.89	9:30	9:30	63	47	<u>0.023</u>	<u>0.017</u>

1023 'a' means NPF event observed at both stations, 'b' means NPF event day at UB station while  
1024 non-event day at MT station, 'c' means NPF event day at MT station while non-event day at UB  
1025 station, 'd' means non-event day at both stations on the same day, 'e' means undefined day at both  
1026 stations, 'f' means undefined day at UB station while NPF event day at MT station, g means  
1027 undefined day at MT station while NPF event day at UB station, h means undefined day at UB station  
1028 while non-event day at MT station, \* means NPF event observed at MT station was transported from  
1029 somewhere else. – means the values cannot be reliably calculated. Only days when particle number  
1030 size distribution were valid are included in this table.

1031



1032

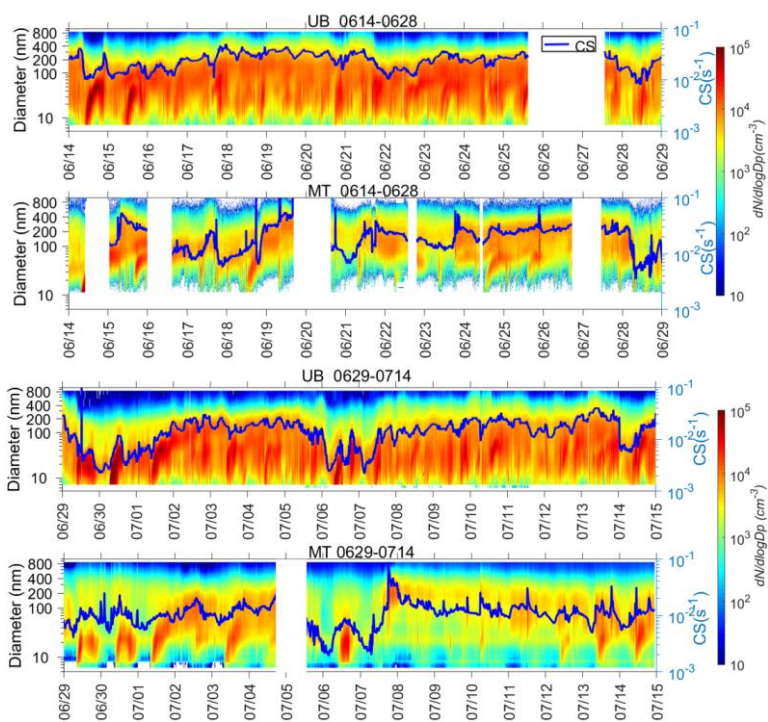


1033

1034 **Figure 1:** Map showing locations of urban station (UB), Longquan station (LQ), and  
1035 mountain station (MT) and another site 60 km south from MT station (S60). The S60 referred  
1036 to the location where particles formed during the non-local NPF event observed at MT station  
1037 on June 15, 2019. Image is produced using © Google Maps.

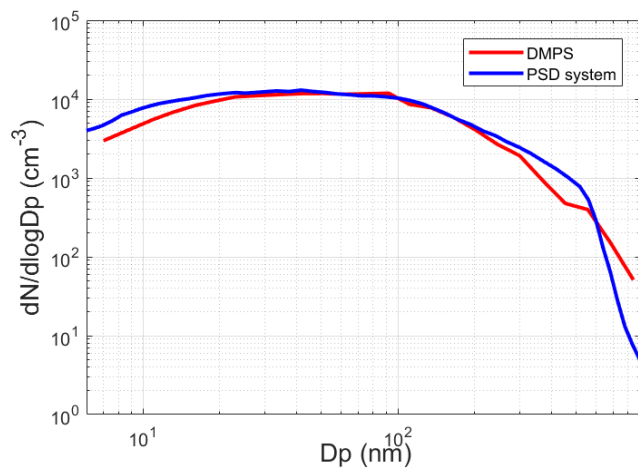
1038

1039

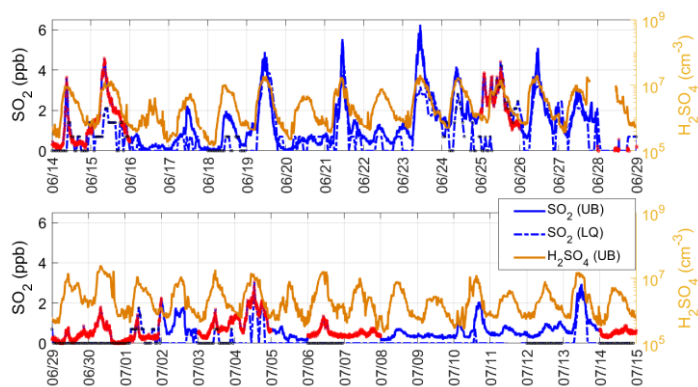


1040  
 1041 **Figure 2:** Time series of particle number size distribution and CS (the blue line) at UB and  
 1042 MT stations during our observations. Time resolutions for particle number size distribution  
 1043 data and CS were 8 min at UB station and 4 min at MT station, respectively.

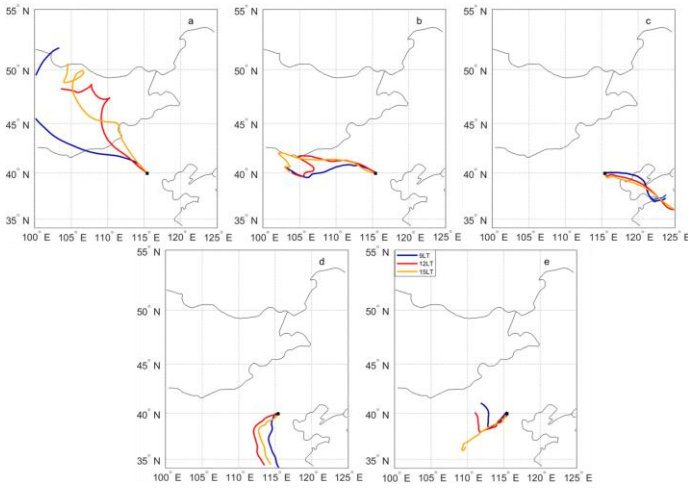
1044  
 1045



1046  
 1047 **Figure 3:** Median particle number size distribution in 5-900 nm measured by DMPS and PSD  
 1048 during our observation from June 1 to August 31, 2019 at UB station. The time window of  
 1049 the data is from 9:00-15:00 of every day.



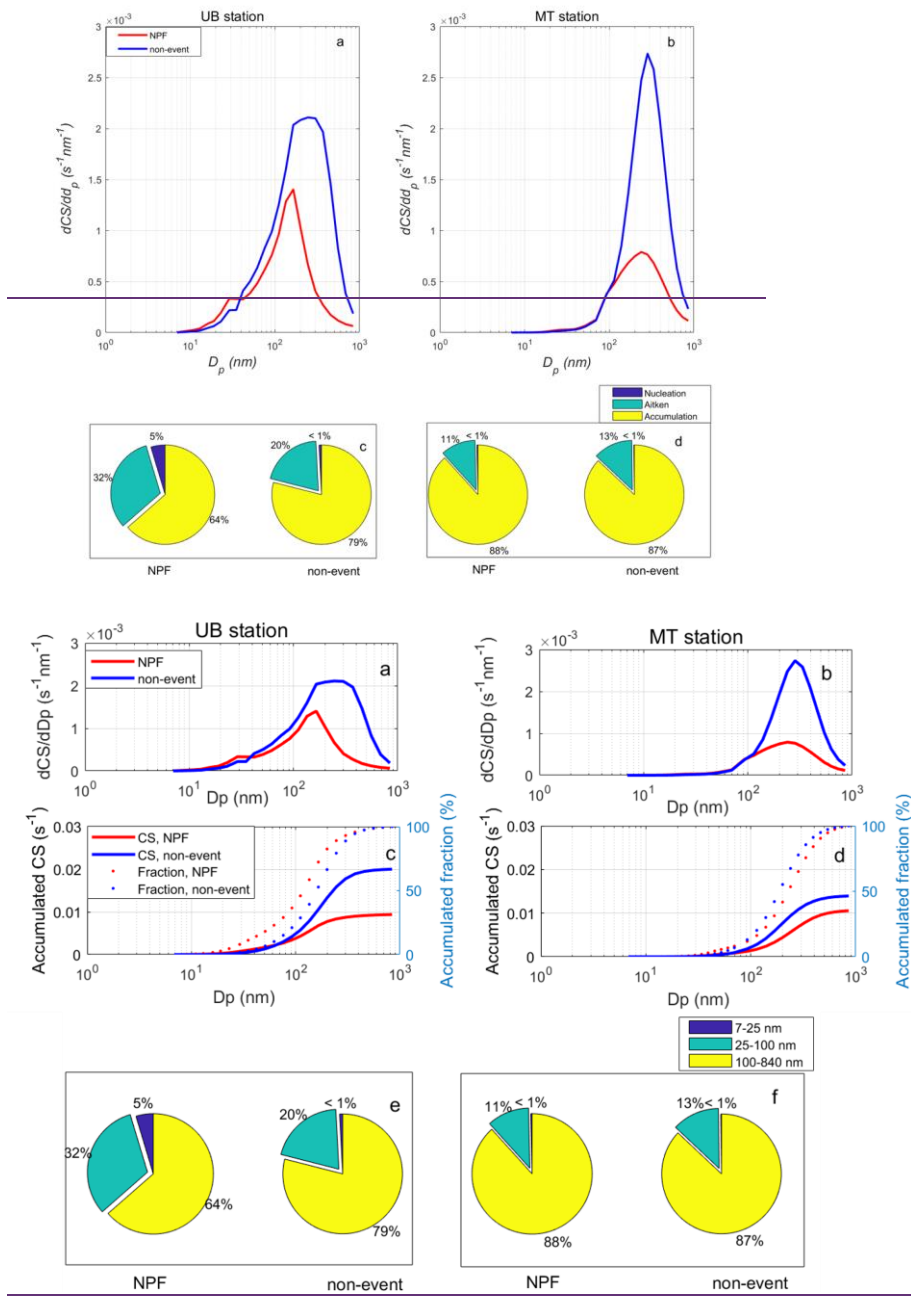
1050  
 1051 **Figure 4:** Time series of SO<sub>2</sub> concentration (ppb) at UB station and Longquan station (LQ)  
 1052 during our observation (left axis) as well as H<sub>2</sub>SO<sub>4</sub> concentration measured at UB station  
 1053 (right axis). Data under detection limit are set as zero at both stations. Data on NPF event  
 1054 days were marked in red at UB station and black at MT station. Time resolution for SO<sub>2</sub> data  
 1055 was 5 min at UB station and 1h at LQ station, respectively.  
 1056



1057  
 1058 **Figure 5:** Examples of air masses arrived at both stations from (a) North group, (b) West  
 1059 group, (c) East group, (d) South group and (d) Local group during 9:00-15:00 (local time, LT).  
 1060 Both stations are under the same marker.

1061  
 1062  
 1063

1064



1065

1066

1067

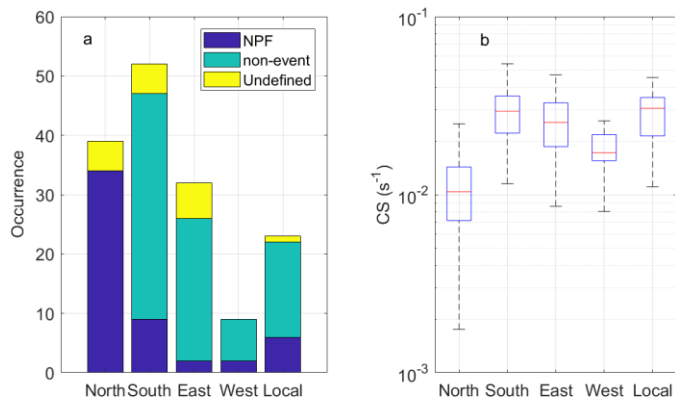
**Figure 6:** Median CS size distribution at UB (a) and MT (b) stations on NPF event and non-event days, respectively during 9:00-15:00 (local time, LT) and median contribution of non-event days, respectively during 9:00-15:00 (local time, LT) and median contribution of non-event days, respectively during 9:00-15:00 (local time, LT).

1068 ~~nucleation, Aitken and accumulation mode particles to total CS at UB (c) and MT (d) stations~~  
1069 ~~on NPF event and non-event days, respectively during 9:00-15:00 (local time, LT). The~~  
1070 ~~time resolutions for CS and particle number concentration data were 8 min at UB station and~~  
1071 ~~4 min at MT station, respectively. Median CS size distribution (a&b), accumulated CS~~  
1072 ~~contributed by particles from 6 nm and the ratio between accumulated CS and total CS (c&d);~~  
1073 ~~Contribution of size-segregated particles to total CS (e&f) at each site on NPF and non-event~~  
1074 ~~days during 9:00-15:00 (local time, LT). Figures on the left and right panels represented data~~  
1075 ~~observed at UB and MT site, respectively. The time resolutions for CS and particle number~~  
1076 ~~concentration data were 8 min at UB station and 4 min at MT station, respectively.~~

1077

1078

1079

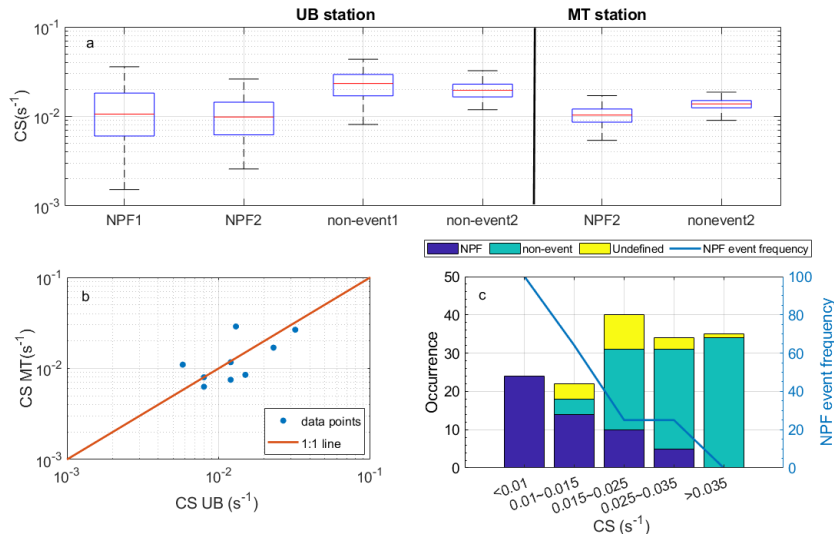


1080

1081 **Figure 7:** Occurrence of NPF events and non-events under air masses arriving from different  
 1082 directions (a) as well as medians and percentiles of condensation sink ( $CS, s^{-1}$ ) during the  
 1083 9:00-11:00 (local time) under different air masses (b) during our observation in summer 2018  
 1084 and 2019 at UB station. The red line represents the median of the data and the lower and  
 1085 upper edges of the box represent 25<sup>th</sup> and 75<sup>th</sup> percentiles of the data, respectively. The length  
 1086 of the whiskers represents  $1.5 \times$  interquartile range which includes 99.3% of the data. Data  
 1087 outside the whiskers are considered outliers and are marked with red crosses. The time  
 1088 resolution of CS was 8 min.

1089

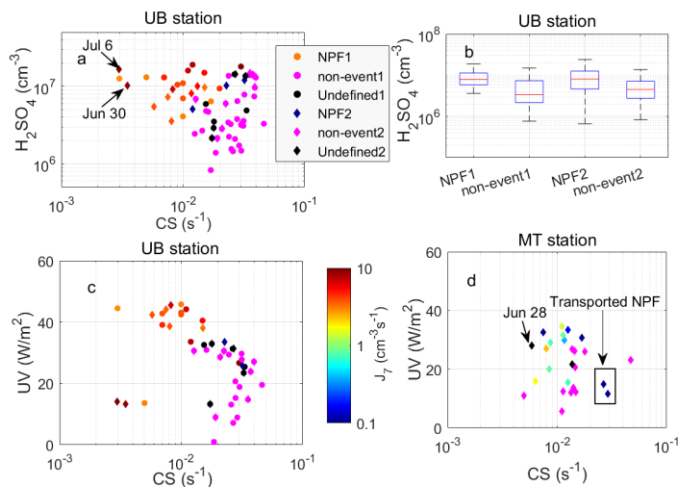




1090

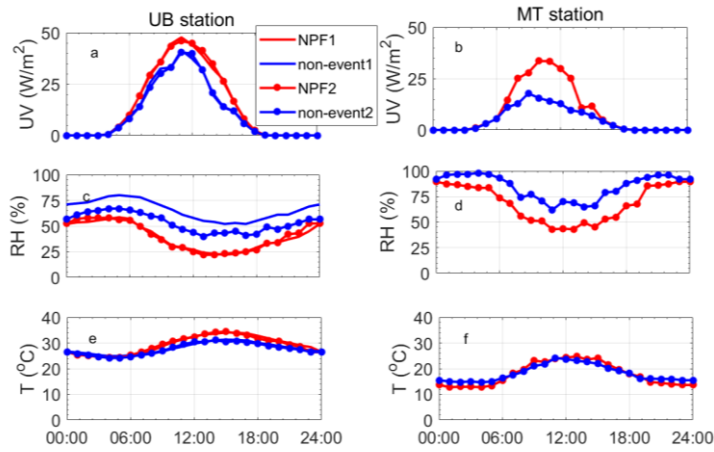
1091 **Figure 8:** (a) Median and percentiles of condensation sink (CS, s<sup>-1</sup>) during our observations  
 1092 at both stations. The ‘NPF1’ and ‘non-event1’ referred to NPF and non-event days during  
 1093 summer 2018 and 2019, while ‘NPF2’ and ‘non-event2’ referred to NPF and non-event days  
 1094 during the short-term parallel observation from June 14 to July 14, 2019 at both sites. The red  
 1095 line represents the median of the data and the lower and upper edges of the box represent 25<sup>th</sup>  
 1096 and 75<sup>th</sup> percentiles of the data, respectively. The length of the whiskers represents 1.5×  
 1097 interquartile range which includes 99.3% of the data. The time resolution of CS was 8 min. (b)  
 1098 Median CS during the first 2 hours of NPF events on common NPF event days measured at  
 1099 both stations (MT vs. UB) . (c) Numbers of NPF event, non-event and undefined days as well  
 1100 as NPF event frequency as a function of CS during our observation in summer 2018 and 2019  
 1101 at UB station.

1102



1103  
 1104 **Figure 9:** (a) Median condensation sinks ( $CS, s^{-1}$ ) and  $H_2SO_4$  concentration ( $SA, cm^{-3}$ ) and (b)  
 1105 (b) medians and percentiles of  $H_2SO_4$  concentration observed at UB station during the first 2  
 1106 hours of NPF events and 9:00-11:00 on non-event days. (c) solar radiation (UVA+UVB,  
 1107  $W/m^2$ ) during the first 2 hours of every NPF event and 9:00-11:00 on every non-event day at  
 1108 UB station. The ‘NPF1’ and ‘non-event1’ referred to NPF event and non-event days in  
 1109 summer 2018 and 2019 and the ‘NPF2’ and ‘non-event2’ referred to NPF event and  
 1110 non-event days during the observation from June 14 to July 14, 2019. (d) Median  
 1111 condensation sinks ( $CS, s^{-1}$ ) and solar radiation (UVA+UVB,  $W/m^2$ ) during the first 2 hours  
 1112 of every NPF event and 9:00-11:00 on every non-event day at MT station. Transported NPF  
 1113 event cases and one non-event day with air masses belonging to west group (Jun 28) were all  
 1114 pointed out in the figure. Size of data points on NPF event days means ~~particle~~ particle-formation rate  
 1115 ( $J_7, cm^{-3}s^{-1}$ ) when it can be calculated reliably. The time resolution of CS was 8 min at UB  
 1116 station and 4 min at MT station, respectively. The time resolution was 30 min for SA data at  
 1117 UB station and 1h for solar radiation data at both stations.

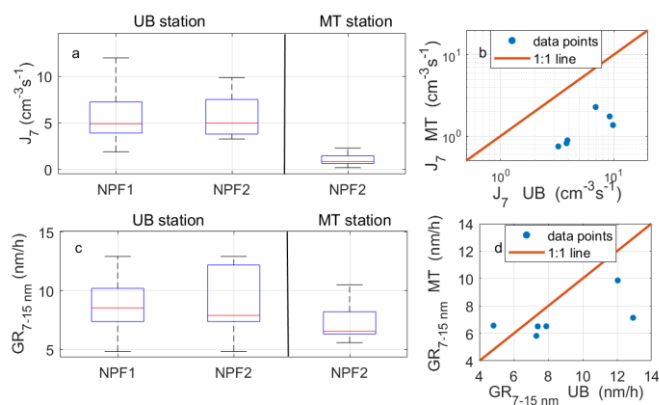
1118  
 1119



1120

1121 **Figure 10:** (a, b) Diurnal pattern of solar radiation (UV, W/m<sup>2</sup>), (c, d) Temperature (T, °C),  
 1122 and (e, f) Relative humidity (RH, %), at UB (left panel) and MT (right panel) stations on both  
 1123 NPF event and non-event days. Time resolutions for all data points here were 1h. The ‘NPF1’  
 1124 and ‘non-event1’ referred to NPF event and non-event days in summer 2018 and 2019 and  
 1125 the ‘NPF2’ and ‘non-event2’ referred to NPF event and non-event days during the  
 1126 observation from June 14 to July 14, 2019.

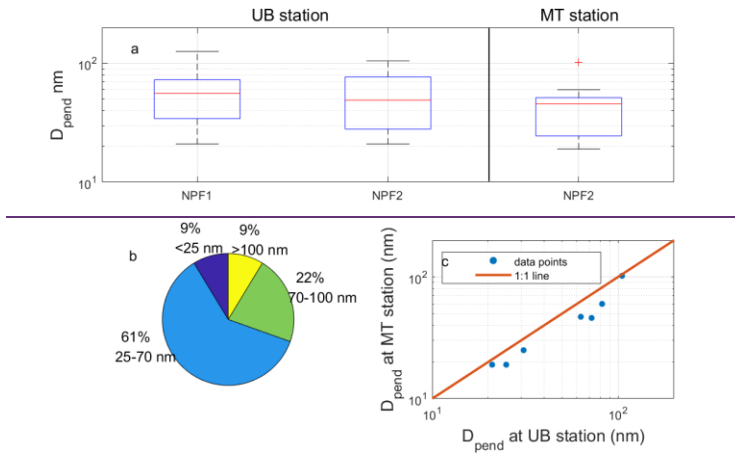
1127



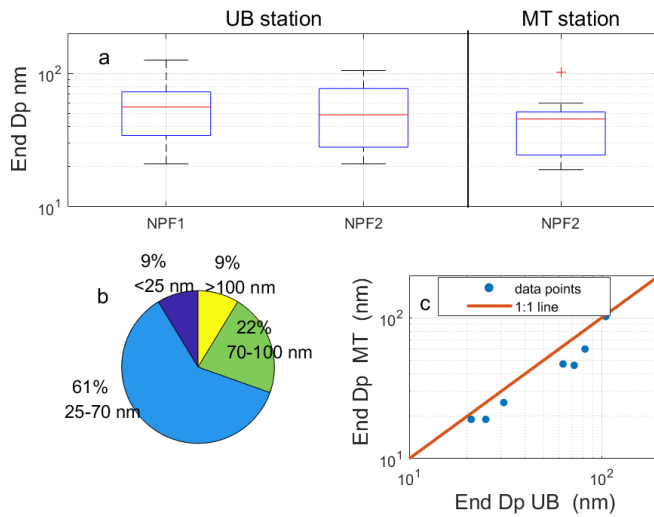
1128  
 1129 **Figure 11:** Median and percentages of ~~particle~~ formation rates of 7 nm ( $J_7$ ,  $\text{cm}^{-3}\text{s}^{-1}$ ) (a) and  
 1130 ~~particle~~ growth rates from 7 to 15 nm ( $\text{GR}_{7-15 \text{ nm}}$ ,  $\text{nm/h}$ ) (c) measured at both stations during  
 1131 our observation as well as comparison between  $J_7$  (b) and  $\text{GR}_{7-15 \text{ nm}}$  (d) of common NPF  
 1132 events. The red line represents the median of the data and the lower and upper edges of the  
 1133 box represent 25<sup>th</sup> and 75<sup>th</sup> percentiles of the data, respectively. The length of the whiskers  
 1134 represents  $1.5\times$  interquartile range which includes 99.3% of the data. The ‘NPF1’ and  
 1135 ‘non-event1’ referred to NPF event and non-event days in summer 2018 and 2019 and the  
 1136 ‘NPF2’ and ‘non-event2’ referred to NPF event and non-event days during the observation  
 1137 from June 14 to July 14, 2019.

1138

1139

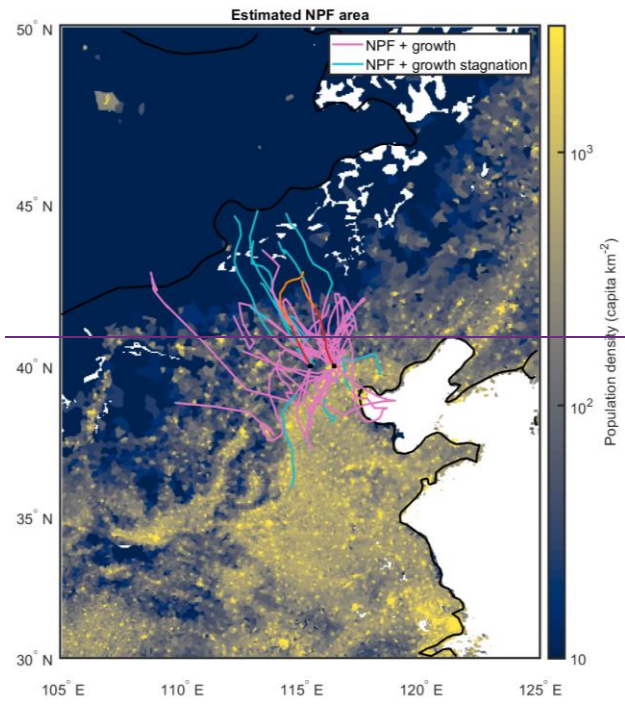


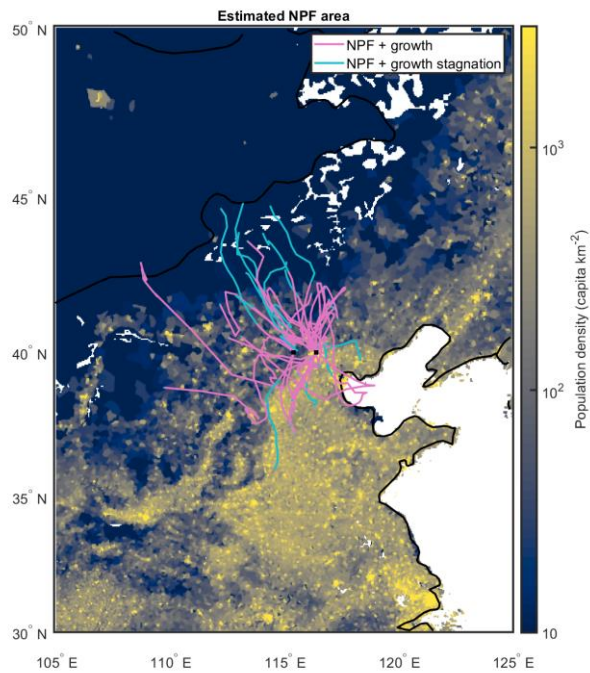
1140



1141 Figure 12: (a) Median and percentiles of end diameters ( $D_{pend}$ , End Dp, nm) of NPF events  
 1142 measured at both sites. The red line represents the median of the data and the lower and upper  
 1143 edges of the box represent 25<sup>th</sup> and 75<sup>th</sup> percentiles of the data, respectively. The length of the  
 1144 whiskers represents 1.5× interquartile range which includes 99.3% of the data. The ‘NPF1’  
 1145 and ‘non-event1’ referred to NPF event and non-event days in summer 2018 and 2019 and  
 1146 the ‘NPF2’ and ‘non-event2’ referred to NPF event and non-event days during the  
 1147 observation from June 14 to July 14, 2019. (b) Frequencies of end diameters in the size range

1148 of smaller than 25 nm, 25-70 nm, 70-100 nm and above 100 nm during our observation at UB  
1149 station in summer 2018 and 2019. (c) Comparison between end diameters of common NPF  
1150 events at both stations.  
1151





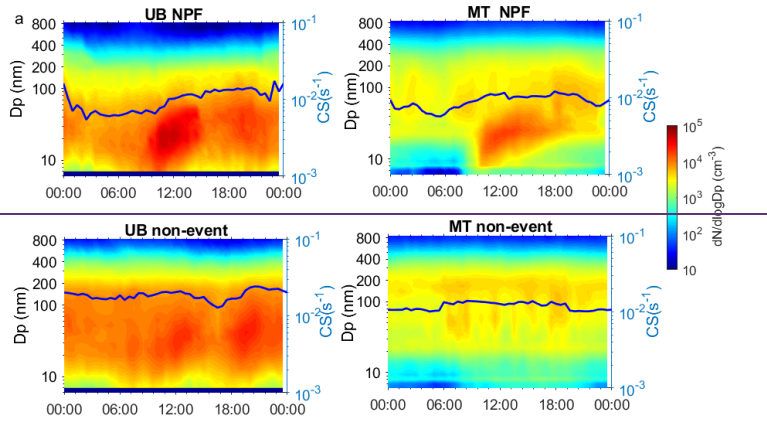
1153  
1154

1155 **Figure 13:** Spatial extent of the area where new particle formation events are estimated to  
 1156 have taken place based on air mass back trajectories and the observed NPF events at both  
 1157 sites. Each line represents a single NPF event and extends to the point beyond which  
 1158 continuation of the mode formed in an NPF event was no longer observed at the  
 1159 measurement site. In other words, if an air mass is located outside the area roughly outlined  
 1160 by the colored lines during the typical onset time of NPF and then transported to our  
 1161 measurement sites, NPF is unlikely to have occurred in said air mass. The lines change color  
 1162 from pink to light blue if the observed NPF event enters a stage of growth stagnation, which  
 1163 can indicate a less favorable environment for the formation and growth of new particles. ~~The~~  
 1164 ~~lines for the case study day of June 30, 2019 are marked with red and change color to orange~~  
 1165 ~~if growth stagnation occurs.~~ The lines are overlaid on top of a population density map  
 1166 (Gridded Population of the World; GPWv4.10; CC BY 4.0), which is used to illustrate the

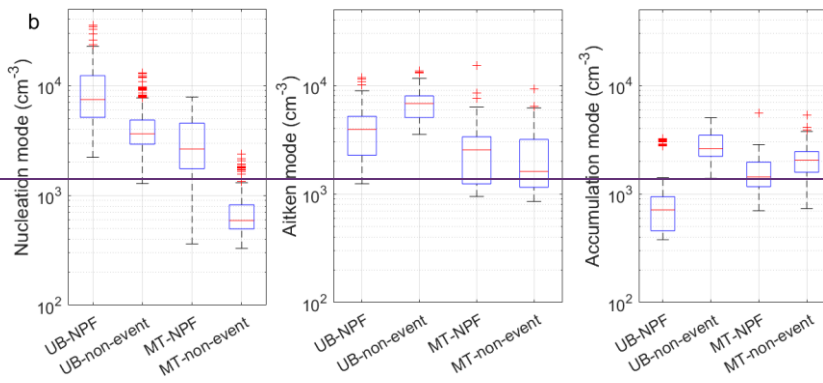


1167 level of anthropogenic activities and emissions.

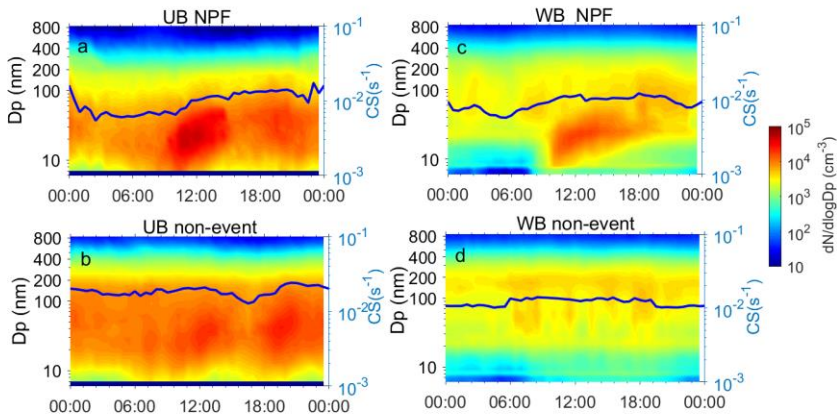
1168



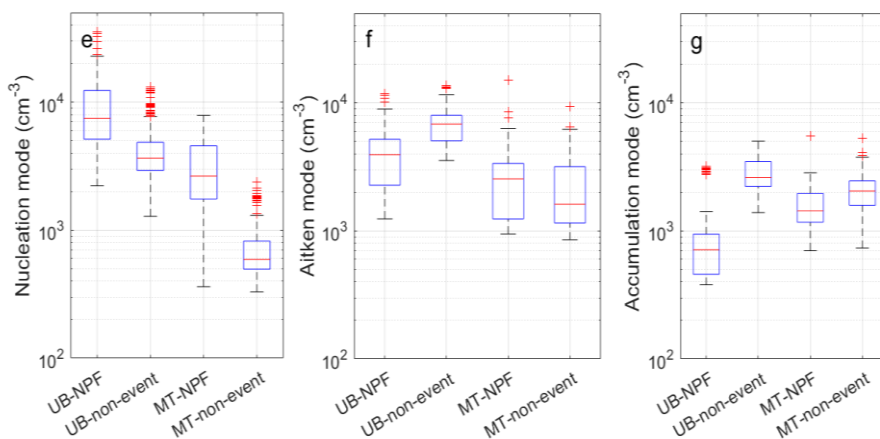
169



170



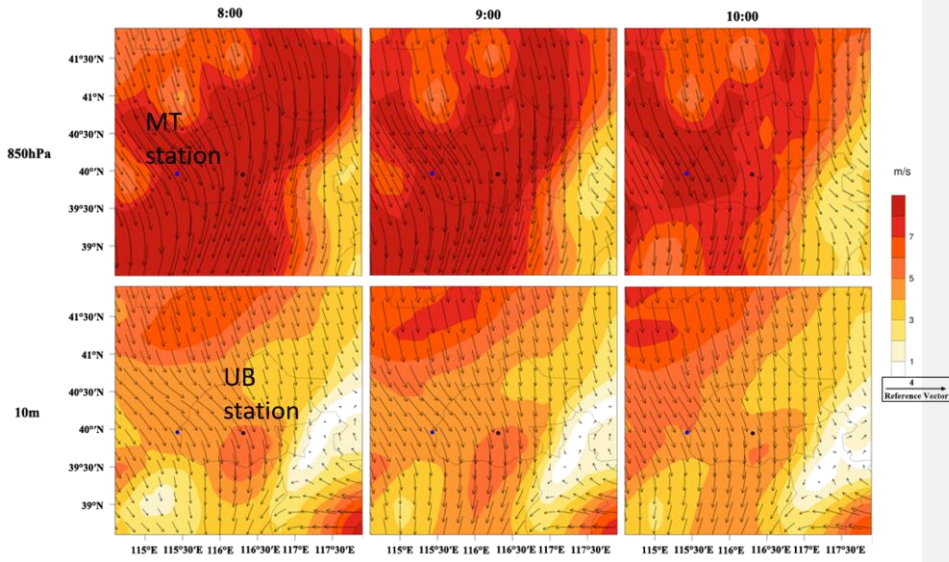
171



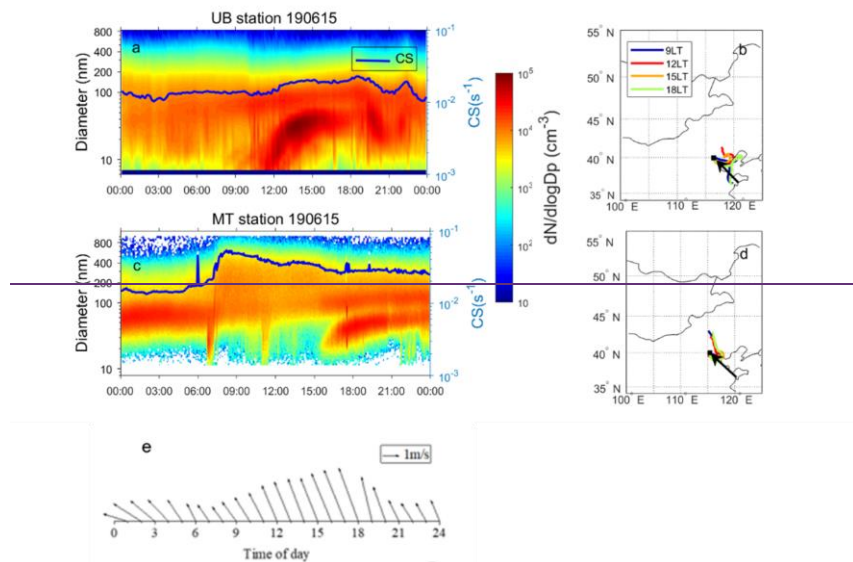
1172  
 1173 **Figure 14:** Median particle number size distribution as well as CS (blue lines) on NPF event  
 1174 and non-event days at UB (a&b) and MT (c&d) stations and median and percentiles of  
 1175 nucleation (e), Aitken (f) and accumulation (g) modes particle number concentration on NPF  
 1176 event and non-event days during our observation from June 14 to July 14, 2019 at both  
 1177 stations. The red line represents the median of the data and the lower and upper edges of the  
 1178 box represent 25<sup>th</sup> and 75<sup>th</sup> percentiles of the data, respectively. The length of the whiskers  
 1179 represents 1.5× interquartile range which includes 99.3% of the data. Data outside the  
 1180 whiskers are considered outliers and are marked with red crosses.

1181  
 1182 **Figure 14:** (a) Median particle number size distribution as well as CS (blue lines) on NPF  
 1183 event and non event days at UB (left panel) and MT (right panel) stations and (b) median and  
 1184 percentiles of nucleation, Aitken and accumulation modes particle number concentration on  
 1185 NPF event and non event days during our observation from June 14 to July 14, 2019 at both  
 1186 stations. The red line represents the median of the data and the lower and upper edges of the  
 1187 box represent 25<sup>th</sup> and 75<sup>th</sup> percentiles of the data, respectively. The length of the whiskers  
 1188 represents 1.5× interquartile range which includes 99.3% of the data. Data outside the  
 1189 whiskers are considered outliers and are marked with red crosses.

1190

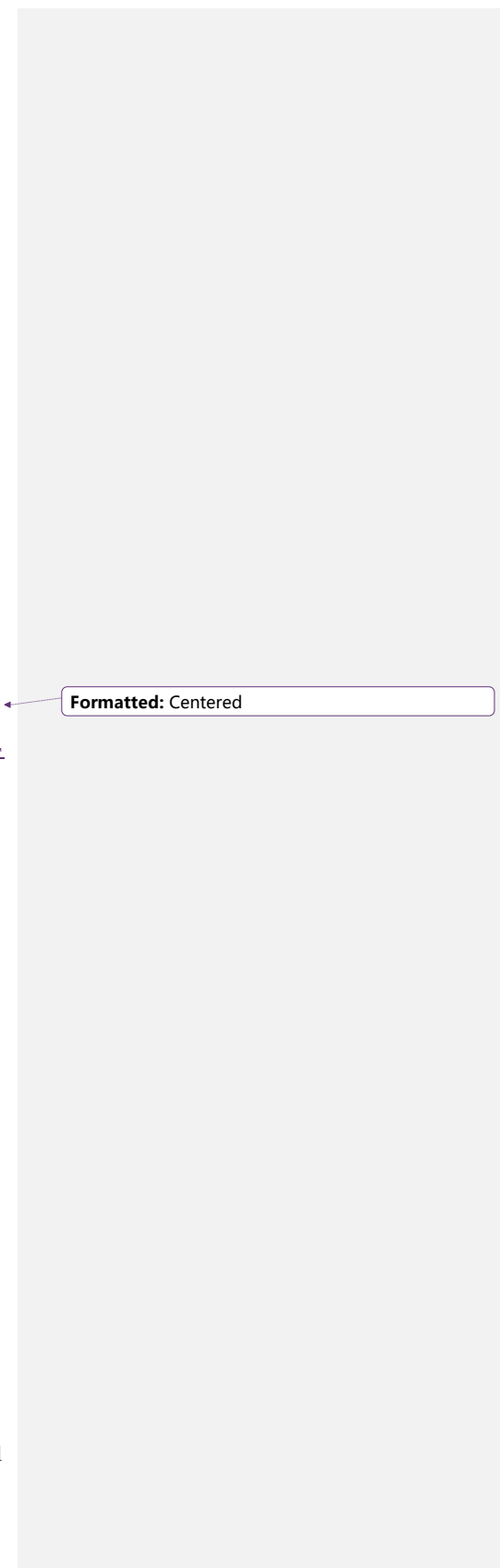


1192  
 1193 Figure 15: Wind distribution at 8:00, 9:00 and 10:00 on June 30, 2019 at 10 m above the  
 1194 ground level (lower panel) and 850 hPa (close to the altitude of MT station, upper panel). The  
 1195 blue and black points on the figures represent MT and UB stations, respectively.  
 1196

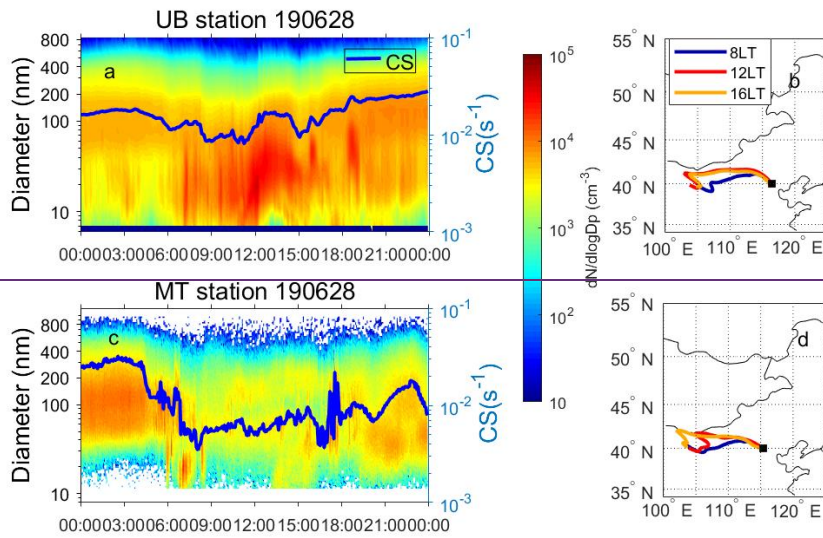


1197  
1198  
1199  
1200  
1201  
1202  
1203

**Figure 16:** Time series of particle number size distribution, CS (blue lines) and air masses arrived at UB (upper panel) and MT (bottom panel) stations as well as wind conditions at MT station on June 15, 2019. Time resolution for particle number size distribution data and CS were both 8 min at UB station and 4 min at MT station, respectively. Time resolution for wind condition data was 1h at MT station. The arrows in the figure denotes directions of prevailing air masses before arriving at both stations during 9:00–15:00 LT.

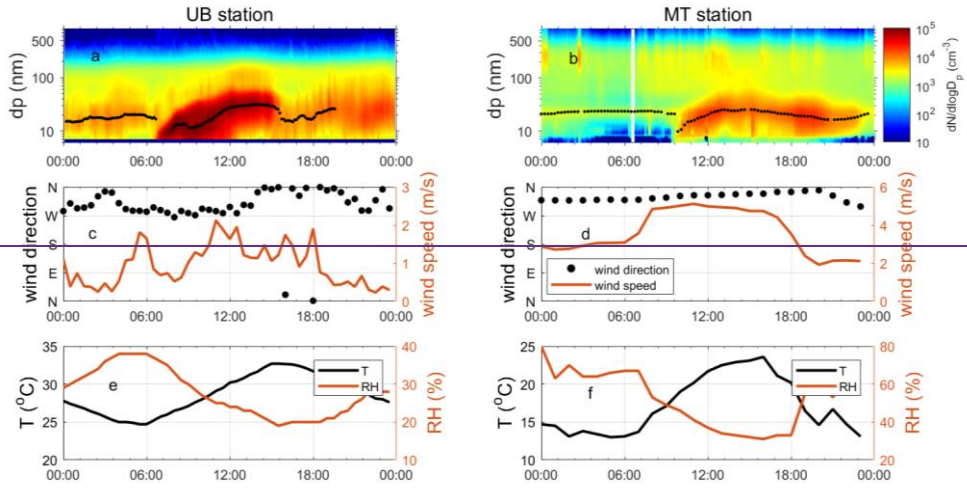


Formatted: Centered



1204  
 1205 **Figure 17:** Time series of particle number size distribution, CS and air masses arrived at UB  
 1206 (upper panel) and MT (bottom panel) stations on June 28, 2019. Time resolution for particle  
 1207 number size distribution data and CS were both 8 min at UB station and 4 min at MT station,  
 1208 respectively.  
 1209

1210



1211

1212

1213 Figure 18: Time-series of particle number size distribution and mode diameters (a, b), wind  
1214 speed and direction (c, d), temperature and RH (e, f) measured at UB (left panel) and MT  
1215 (right panel) on June 30, 2019.